

## Kinematics of the Kahramanmaraş triple junction and of Cyprus: evidence of shear partitioning

Volkan Özbey<sup>1,2,\*</sup>, Ali Mehmet Celâl Sengör<sup>3,4</sup>, Pierre Henry<sup>2</sup>, Mehmet Sinan Özeren<sup>5</sup>, A. John Haines<sup>6</sup>, Elliot C. Klein<sup>7</sup>, Ergin Tari<sup>1</sup>, Cengiz Zabcı<sup>3</sup>, Konstantinos Chousianitis<sup>8</sup>, Sezim Ezgi Güvercin<sup>9</sup> and Nazik Öğretmen<sup>5,a</sup>

<sup>1</sup> Istanbul Technical University, Department of Geomatics Engineering, 34469 Maslak, Istanbul, Turkey

<sup>2</sup> Aix-Marseille Université, CNRS, IRD, INRA, Coll France, CEREGE, Aix-en-Provence, France

<sup>3</sup> Istanbul Technical University, Department of Geology, 34469 Maslak, Istanbul, Turkey

<sup>4</sup> Center for Global Tectonics, School of Earth Sciences, State Key Lab for Geological Processes and Mineral Resources, Badong National Observatory and Research Station for Geohazards, China University of Geosciences, Wuhan, China

<sup>5</sup> Istanbul Technical University, Eurasia Institute of Earth Sciences, 34469 Maslak, Istanbul, Turkey

<sup>6</sup> GNS Science, Institute of Geological and Nuclear Sciences Ltd, Lower Hutt, New Zealand

<sup>7</sup> FM Global, Research Division, Norwood, MA, USA

<sup>8</sup> Institute of Geodynamics, National Observatory of Athens, Lofos Nymfon, Athens, Greece

<sup>9</sup> Yıldız Technical University, Department of Geomatics Engineering, 34349 İstanbul, Turkey

Received: 9 January 2024 / Accepted: 30 May 2024 / Publishing online: 23 August 2024

**Abstract** – Triple junctions involving convergent plate boundaries extend beyond local implications, which is crucial for studying the geology of convergent plate boundary zones. However, kinematic models overlook Cyprus-Anatolia motion due to limited geodetic constraints. Our study area comprises Cyprus, southern Turkey, and the Levant coast, focusing on the Kahramanmaraş triple junction, where a destructive earthquake sequence occurred on February 6, 2023. We present precise positioning data merged with published velocities, constructing an up-to-date velocity field for the interseismic period. Employing two kinematic approaches, we analyze its tectonic implications. In Cyprus, we find the relative motion of Africa (Sinai Plate) and Anatolia is partitioned between convergence in the Cyprus subduction, with a rate of 3.5–6.2 mm/yr, progressively decreasing from west to east and left-lateral transpressive Kyrenia fault, situated along the northern coast of Cyprus, with rate 3.3–4.2 mm/yr. The relative strike-slip motion between Arabia and Anatolia is partitioned between the East Anatolian Fault (slip rates 5.2–6.2 mm/yr) and some secondary faults such as Çardak and Malatya faults (slip rates 2.0–1.7 mm/yr respectively) and causes distributed deformation for a 50–60 km wide region. The largest second invariant strain rate tensors from the continuum kinematic model also coincide with the same region, the East Anatolian shear zone. A shear partitioning system exists around the Kahramanmaraş triple junction, from Cyprus to southeast Turkey. The Levant Fault has a 3.5–4.7 mm/yr left-lateral slip rate, decreasing northward as part of it is transferred to offshore faults. Strain rates appear relatively small in the Taurus range and Adana/Cilicia basin, transitioning from extensional/transensional to compressional from east to west.

**Keywords:** Kahramanmaraş triple junction / Kinematic modelling / Shear partitioning / Cyprus Subduction zone / East Anatolian shear zone / Kahramanmaraş earthquake doublet

**Résumé** – La déformation associée aux jonctions triples impliquant des plaques convergentes s'étend régionalement et influe sur l'activité sismique et l'évolution tectonique des frontières de plaque. Notre étude de la jonction triple de Kahramanmaraş—où une séquence de tremblements de terre destructeurs s'est produite le 6 février 2023—englobe Chypre, le sud de la Turquie et la côte du Levant. Nous fusionnons de nouvelles données de positionnement GNSS avec les champs de vitesses publiées, construisant ainsi un champ de vitesse intersismique incluant Chypre—où les données disponibles étaient jusqu'à présent très

<sup>a</sup> Now at Center for Marine Sciences, University of Algarve, Faro, Portugal

\*e-mail: [ozbeyv@itu.edu.tr](mailto:ozbeyv@itu.edu.tr)

limitées. Ce champ de vitesse est analysé d'une part avec un modèle de blocs élastiques et d'autre part avec une méthode d'interpolation continue. Nous montrons que le mouvement relatif de l'Afrique (plaque Sinaï) et de l'Anatolie est partitionné entre la subduction de Chypre, avec un taux de convergence de 3,5 à 6,2 mm/an diminuant progressivement d'ouest en est, et la faille transpressive de Kyrenia, situé le long de la côte nord de Chypre, avec une vitesse de décrochement senestre 3,3 à 4,2 mm/an. Ce système de partitionnement se prolonge à terre où le mouvement de décrochement entre l'Arabie et l'Anatolie est réparti dans une zone de cisaillement de 50 à 60 km de large. Dans la zone des séismes du 6 février ce mouvement est distribué entre la Faille Est Anatolienne (taux de glissement 5,2–6,2 mm/an) et certaines failles secondaires telles que les failles Çardak et Malatya (taux de glissement 2,0–1,7 mm/an). Entre les plaques Arabie et Sinaï, la faille du Levant a un taux de glissement senestre de 3,5 à 4,7 mm/an, diminuant vers le nord ou une partie de la déformation est transférée en mer. Il apparaît ainsi que le mouvement sur chacune des frontières de plaques formant la jonction triple de Kahramanmaraş est réparti sur plusieurs failles. En revanche, les taux de déformation sont relativement faibles dans la chaîne du Taurus et dans le bassin d'Adana/Cilicie où le style de déformation change progressivement d'extensif/transensif à l'est à transpressif à l'ouest.

**Mots clés :** Jonction triple de Kahramanmaraş / Modélisation cinématique / Cisaillement / Zone de subduction chypriote / Faille est-anatolienne / Doublet sismique de Kahramanmaraş

## 1 Introduction

The recent tectonics of the Eastern Mediterranean result from the interaction of the Arabia, Africa, and Eurasia plates since Miocene (McKenzie, 1972; McKenzie *et al.*, 1970; Biddle, 1985; Fig. 1a). During the middle Miocene, Arabia was separated from Africa along the left-lateral Levant (or Dead Sea) fault zone (*e.g.*, Le Pichon and Francheteau, 1978). The subsequent collision of Arabia with Europe, resulting in gravitational potential build-up in Eastern Anatolia, combined with an acceleration of slab rollback in the Hellenic subduction where the northern African slab is subducted (Brun *et al.*, 2016) and a possible contribution from underlying asthenospheric flow, have been driving the westward extrusion of the Anatolian Plate (Le Pichon and Kreemer, 2010; Özeren and Holt, 2010). Currently, the boundary between Arabia and Anatolia is a left lateral transform plate boundary, the East Anatolian Fault zone (EAF) (McKenzie, 1976). Africa has been divided in the Eastern Mediterranean into a Nubia plate (Le Pichon and Gaulier, 1988; McKenzie *et al.*, 1970) and a Sinai sub-plate (Mahmoud *et al.*, 2005). The Sinai plate thus subducts beneath Anatolia along the Cyprus Arc and moves southward concerning Arabia along the Levant Fault zone. The Kahramanmaraş triple junction is the junction of the Levant Fault zone, the East Anatolian Fault zone (EAF), and the Cyprus Arc Subduction (Karig and Kozlu, 1990; Sengör *et al.*, 1980, 1985) (Fig. 1b). This triple junction also gives rise to a very complex pattern of deformation in the northeastern Mediterranean because of the convergence of the two continental plates, namely Arabia and Anatolia. Additionally, the marine part of the Sinai Plate is formed of thinned continental crust, comprising a thicker region, the Eratosthenes seamount, which is currently impinging the Cyprus Arc (Le Pichon, 2019). In this incipient collision, the relative motion of Sinai and Anatolia is distributed between the Cyprus Arc subduction, the Kyrenia fault running along the Northern Coast of Cyprus, and the Taurus range onshore further north. In fact, two triple junctions are currently active in the area, namely those of Hatay (see Fig. 1b) where the eastward prolongation of the Cyprus arc reaches the Levant Fault, and Kahramanmaraş where the NE prolongation of the Kyrenia fault reaches

the EAF (Sengör *et al.*, 2019; Özkan *et al.*, 2023). However, the motion of Cyprus with respect to Anatolia has been ignored so far in regional kinematic models because of a lack of constraints from geodesy, due to insufficient data on the island (see for example Mahmoud *et al.*, 2005; Reilinger *et al.*, 2006; Gomez *et al.*, 2020).

This paper presents a refined GNSS (Global Navigation Satellite Systems) velocity field encompassing southern Turkey and Cyprus. Leveraging these data, we construct regional kinematic models that not only illuminate the motion of the study area but also incorporate higher-resolution boundary conditions and internal deformation characteristics specific to Cyprus. Through these novel data and models, we foster a more comprehensive understanding of the neotectonics of the northeastern Mediterranean. In addition, we will discuss the kinematic context of the major earthquakes that occurred in the Kahramanmaraş triple junction area on February 6, 2023: Mw (moment magnitude) 7.8 Pazarck earthquake on the EAF and Mw 7.6 Elbistan earthquake on Çardak Fault (Barbot *et al.*, 2023; Hussain *et al.*, 2023).

Previous geodetic studies either measured Arabia and Anatolia plate motion and deformation (Bletery *et al.*, 2020; Cavalié and Jónsson, 2014; England *et al.*, 2016; Kurt *et al.*, 2022; Özeren and Holt, 2010; Reilinger *et al.*, 2006; Viltres *et al.*, 2022; Weiss *et al.*, 2020) or focused on the kinematics of the Levant fault zone (Al Tarazi *et al.*, 2011; Alchalbi *et al.*, 2010; Gomez *et al.*, 2020; Gomez *et al.*, 2007; Hamiel and Piatibratova, 2021; Le Beon *et al.*, 2008; Sadeh *et al.*, 2012) and of the East Anatolian fault zone (Bletery *et al.*, 2020; Cavalié and Jónsson, 2014; Walters *et al.*, 2014). However, only a few studies account for the active deformation of secondary faults such as Malatya and Çardak Faults (also called Sürgü Fault by some authors) (Westaway, 2003), or the Karatas-Osmaniye Fault (Mahmoud *et al.*, 2013; Özkan *et al.*, 2023). Ascertaining the kinematics of the Cyprus Arc Subduction using land-based GNSS observations has proven to be a difficult task since much of the subduction arc is expressed beneath the Mediterranean Sea. The Island of Cyprus is the only place within the Eastern Mediterranean Basin where the Cyprus Arc Subduction kinematics can be studied using onshore geodetic constraints. Still, the data have been too sparse to date. We thus conducted new GNSS surveys

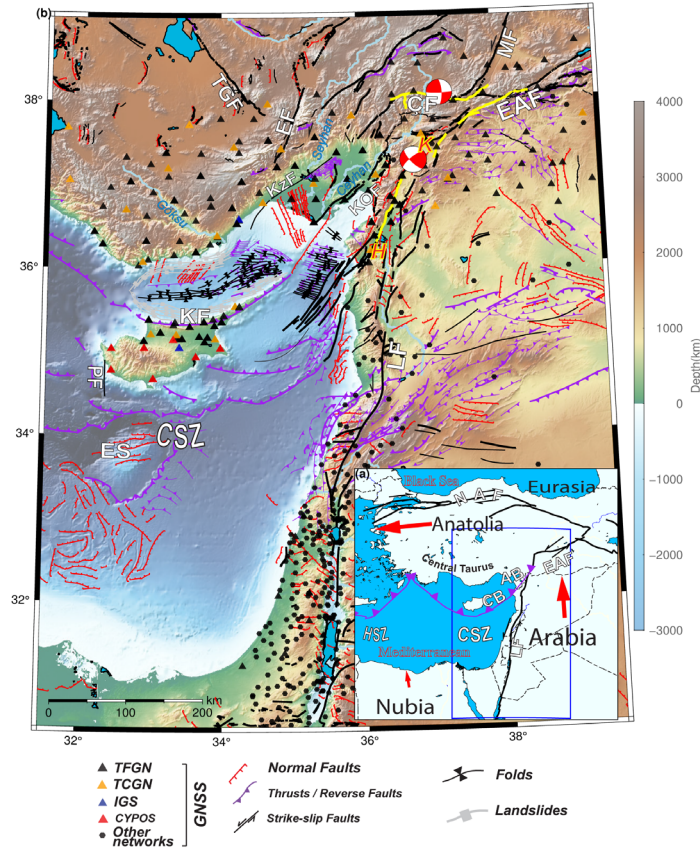


**Fig. 1.** a) Tectonics of the Eastern Mediterranean and fundamental features in the scope of this study. Abbreviations: EAF: East Anatolian Fault, NAF: North Anatolian Fault, LF: Levant Fault, CSZ: Cyprus Subduction Zone, HSZ: Hellenic Subduction Zone, AB: Adana Basin, CB: Cilicia Basin b) Tectonic structures and GNSS sites around the region. Structures digitized from Emre *et al.* (2013, 2018); Şengör and Zabcı (2019), the structures around Adana/Cilicia basins are taken from Aksu *et al.*, 2005; Burton-Ferguson *et al.*, 2005; Aksu *et al.*, 2014a, 2021, and cited studies therein). The main boundaries are represented with thicker lines. Focal mechanisms belong to 06 Feb 2023 Mw=7.8 and Mw=7.6 Kahramanmaraş Pazarcık and Elbistan earthquakes. The surface rupture geometry, shown in yellow lines, is taken from the U.S. Geological Survey (USGS) with Data Release (doi: 10.5066/P98517U2). Abbreviations: K=Kahramanmaraş triple junction, H=Hatay triple junction, KF: Kyrenia Fault, CF: Cardak Fault, MF: Malatya Fault, EF: Ecemiş Fault, KOF: Karatas-Osmaniye Fault, TGF: Tuz Gölü Fault, KZF: Kozan Fault, PF: Paphos Fault, ES: Eratosthenes seamount, IGS: International GNSS Service, TCGN: Turkey Continuous GNSS Network, TFGN: Turkey Fundamental GNSS Network, CYPOS: Cyprus Positioning System. We consistently employ the same abbreviations throughout all figures in this text, adhering to those presented in this figure, as necessary.

in Cyprus between 2019 and 2021, along with data from permanent GNSS sites, providing comprehensive spatial coverage for constructing a kinematic model of the eastern Mediterranean. Our velocity field includes follow-up surveys in the Turkish mainland and velocities published by previous studies. In Section 2 we present our GNSS processing strategy and integration workflow details.

We applied two kinematic inversion methods with our combined velocity field as input. On the one hand, we employed a continuum velocity field interpolation method to calculate the strain rate field of the study area (Beavan and Haines, 2001; Haines and Holt, 1993). This strain distribution may be compared with seismicity distribution and tectonic strain regimes indicated by fault maps. This information also contributes to the definition of boundaries for a block model. The block model calculates rigid block motions and coupling on the block boundaries defined as dislocation sources (McCaffrey *et al.*, 2007). The output of this model may thus

be interpreted in terms of long-term slip rates and seismic coupling on major faults. This model also allows for the internal deformation of the blocks by calculating a unique and uniform strain rate tensor for each block. In parallel,

Our newly acquired data and model results help us to address several important questions regarding the kinematics and active tectonics of the Eastern Mediterranean region. We quantify the partitioning of deformation among the Cyprus Arc Subduction, Kyrenia fault, and Taurus range. We evaluate the distribution of deformation around the Kahramanmaraş and Hatay triple junctions, notably between the EAF and the Karatas-Osmaniye-Çardak-Malatya fault system and discuss implications for earthquake recurrence intervals. Regarding the Levant fault, the present study is based on fewer velocity vectors than, for instance, presented in (Gomez *et al.*, 2020) and has little to add to their demonstration that slip on the main fault strand is decreasing northward toward the triple junction as part of the motion is diverted offshore.

## 2 GNSS observations and analysis

### 2.1 GNSS data

We present a GNSS velocity field that unites newly derived with previously published velocities. We conducted GNSS surveys in Cyprus between 2019 and 2021 and revisited 18 points that had been previously measured in 1998 and 2001. We also incorporated the data from seven permanent GNSS sites in the southern part of the island. For the first time, we now have reasonable spatial coverage of space geodetic data in Cyprus. This enables us to construct a kinematic model of the easternmost Mediterranean that, in turn, provides us with a more detailed picture of the deformation within Cyprus. We also conducted some follow-up surveys at several GNSS survey-mode sites in the Turkish mainland to further constrain the kinematics of Anatolia with better coverage. We then integrated into our velocity field previously published velocities acquired over the vicinity of the Levant fault and EAF.

The raw data of the continuous stations were obtained from both international networks (International GNSS Service – IGS hereafter) and regional networks (Turkey Continuous GNSS Network and Cyprus Positioning System) (Fig. 1b). We primarily analyzed the dataset from 2009 to 2021 for continuous stations, although some of them had data gaps during that period. However, we have approximately 10 years of time series for almost every continuous site. The survey mode GNSS sites were selected from the Turkey Fundamental GNSS Network to utilize valuable existing observations and data resources. Each observation was carried out using dual-frequency receivers and a filtering cut-off angle of 10 degrees to minimize atmospheric noise. Each survey mode site has at least 7 different sessions, except for 3 sites in the northern part of Cyprus that were set up in 2019, and all sessions have at least 8 hours of observations. The readers can find further details of the data span of survey mode sites in the supplementary file. We evaluated the raw data of 137 GNSS stations (65 continuous – 72 survey modes) and estimated their velocities.

### 2.2 Seismicity

The long-term seismicity catalogue between 1905 and 2019 represented in this figure was compiled from Kandilli Observatory and Earthquake Research Institute's seismicity catalogue between 1905 and 2019 (Kandilli *et al.*, 2001; <http://www.koeri.boun.edu.tr>). The magnitude of completeness of the catalogue is  $\sim M_c = 4$ . The mean horizontal location uncertainty is less than 5 km in N-S and E-W directions. The mean of the depth uncertainty is  $\sim 3.5$  km, varying between 2 and 8 km. We filtered the original catalogue based on quality factors such as horizontal location uncertainty  $< 5$  km and RMS  $< 0.5$  s. This dataset does not include the February 2023 earthquakes and their aftershocks. In the East Anatolian shear zone, this data set emphasizes seismic activity on the Malatya Fault (MF), between the Çardak Fault (CF) and Karatas-Osmaniye Fault (KOF), and south of Hatay but displays relatively little activity along and on the recently ruptured segments of Çardak fault and the EAF. A concentration of earthquakes observed south of Cyprus is largely associated

with the subduction plane of the Cyprus Arc and will here be used to constrain its geometry.

### 2.3 Data evaluation

We performed data processing using a combination of GAMIT/GLOBK software (Herring *et al.*, 2018a, and the extensive literature cited therein) and a stochastic approach. GAMIT/GLOBK integrates the double differences method and carrier phase combinations to eliminate geometric and non-dispersive delays in the solution. We used IGS final orbit and clock products as orbit parameters and the VMF1 (Vienna Mapping Function 1) mapping function to minimize the effect of the tropospheric delay (Boehm *et al.*, 2006). In addition, we incorporated over 20 IGS stations into our network to define a well-constrained global network. We processed daily data from 2009 to 2022, while for the period between 1998 and 2009, we only evaluated days with observations for our survey-mode sites. We verified our daily solutions by following the steps outlined in (Herring *et al.*, 1990). Once daily solutions were obtained for each station, combinations were carried out using a Global Kalman filter approach (Herring *et al.*, 2018a). This approach facilitates the sequential estimation of parameters, providing an advantage over other estimation methods due to its ability to define the state vector and its stochastic model for future measurement times (Herring *et al.*, 2018b). Global network solutions from various institutions were integrated into the evaluation to create a comprehensive network encompassing the existing regional one. The time series for all sites were generated relative to the International Terrestrial Reference Frame 2014 (ITRF14) (Altamimi *et al.*, 2016).

The time series analysis was carried out in three main steps. Firstly, outliers were detected and removed, with a particular emphasis on permanent sites due to their extensive data. Secondly, efforts were made to acquire more realistic sigma values for each site. To achieve this, a first-order Gauss-Markov Extrapolation was implemented. Given the substantial differences in data quantity between continuous and survey-mode sites, these steps were executed with multiple approaches. Random walk noise of 0.02 mm/yr was added to all permanent sites' horizontal and vertical components. Conversely, the random walk noise added to survey-mode sites was five times greater. The subsequent step involved generating velocities for each site. The velocity field was determined with respect to the Arabian plate fixed reference frame, utilizing Euler pole parameters from (Altamimi *et al.*, 2017).

Station velocities and uncertainties for each component (North, East) and time span The supplementary document provides the corresponding time series in Tables S1–S3.

### 2.4 Unifying velocity fields

After generating an initial velocity field, we combined our resulting GNSS velocity field with published velocities from previous studies (Gomez *et al.*, 2020; Hamiel and Piatibratova, 2021; Kurt *et al.*, 2022; Viltres *et al.*, 2022; Özkan *et al.*, 2023). To minimize the effect of some well-known sources of noise

**Table 1.** Root mean square fit of the velocity combination. The first column includes the name of the studies and the second column indicates the initial reference frame of each velocity field. The third column shows the number of common station pairs.

Study	Reference frame	No of common stations	RMS (mm/yr)
(Gomez <i>et al.</i> , 2020)	ITRF08	20	0.96
(Hamiel and Piatibratova, 2021)	ITRF14	27	0.46
(Kurt <i>et al.</i> , 2022)	EURA_I14	65	0.57
(Viltres <i>et al.</i> , 2022)	ARAB_I14	13	0.22
(Özkan <i>et al.</i> , 2023)	EURA_I14	23	0.93

such as those stemming from different data evaluation strategies and pre-defined reference frames from different studies, we rotated all velocity fields individually with respect to our dataset.

The rotation is based on a least-square approach that aims to optimize the transformation matrix of common stations for each velocity field pair. Though this approach has been applied in several studies, we made some critical changes to the weight matrix of the objective function (see Özbey *et al.*, 2021, (Eq. (4)). The weight parameter  $r_i$  has been constructed as the function of both distance  $D_i$  between the  $i$ th common site pair, and the number of observations  $n_x$  and  $n_y$  for the two related stations  $x$  and  $y$  (Eq. (1)).

$$r_i = \begin{cases} e^{-D_i^2/n_x*n_y}, & 1 < D_i \leq 5 \\ e^{-1/n_x*n_y}, & D_i \leq 1 \end{cases} \quad (1)$$

Stations with a distance closer than 5 km are considered to be co-located while stations with a distance closer than 1 km are considered to be the same points. In addition, our approach takes into account the plate and block boundaries during its decision-making process. If the related station pair is located on different blocks or plates, the algorithm rejects it. The second parameter that is taken into account is the number of epochs for each site. Here it is important to note that the number of observations of permanent sites has been postulated as 365 for a year. Each velocity field has been rotated separately by taking the velocity field obtained by this study as the reference system. The statistical outcomes of these processes are listed in Table 1.

Figure 2 shows the final velocity field leveraging in the kinematic models. The unified velocities with respect to both the Arabian-fixed and ITRF reference frames, defined from (Altamimi *et al.* 2017), can be found in the supplementary material as Table S4.

### 3 Modelling

We present two different modelling approaches to reveal the present-day kinematics around the Kahramanmaraş triple junction and Cyprus. We first introduce a continuum kinematic model and generate a continuum velocity field to monitor the deformation of the region. We then introduce a block model that describes the rates of interseismic block motions occurring along the block boundaries. We suggest a block geometry for the study area and testing this geometry with previously published models including our own (Klein *et al.*, 2022) that we developed prior to the two devastating earthquakes of

February 2023. Once the best-fitting geometry is determined, we present rotation poles for each block, slip rates, and coupling ratios for the faults. It is important to note that the block model geometry presented herein was defined before 2023 (Klein *et al.*, 2022).

#### 3.1 Strain rate field

Here, we generate a contemporary strain rate field to characterize deformation styles in the region that comprises northeast Nubia, the eastern Mediterranean Sea, the Levant fault, Cyprus, Adana/Cilicia basin, and neighbouring southern Turkey. We aim to shed light on the kinematics of the region therein. This can be useful for future dynamical models as kinematic constraints or for future seismic hazard models as geodetically inferred moment constraints. Our kinematic continuum model is based on the method described by (Beavan and Haines, 2001; Haines and Holt, 1993).

The method is essentially a least-squares fit to the GNSS data. The horizontal velocity field in the interpolation domain is derived from a vector function  $\mathbf{W}(\mathbf{r})$ :

$$\mathbf{v} = \mathbf{W}(\mathbf{r}) \times \mathbf{r} \quad (2)$$

The function  $\mathbf{W}\mathbf{r}$ , in equation (2), is defined at the knotpoints of a quadrilaterals mesh on the spherical earth surface and interpolated with bicubic spline functions (Beavan and Haines, 2001; Haines and Holt, 1993). The  $\mathbf{W}(\mathbf{r})$  values at knotpoints are inverted in order to minimize a penalty function, which in our application case is of the form:

$$\sum_{\text{points}} \sum_{\alpha,\beta} (v_{\alpha}^{\text{fit}} - v_{\alpha}^{\text{obs}}) V_{\alpha,\beta}^{-1} (v_{\beta}^{\text{fit}} - v_{\beta}^{\text{obs}}) + \sum_{\text{cells}} \nu (\bar{\epsilon}_{\phi\phi}^2 + 2\bar{\epsilon}_{\phi\theta}^2 + \bar{\epsilon}_{\theta\theta}^2) S \quad (3)$$

where  $V_{\alpha,\beta}$  represent the data variance-covariance matrices for the geodetic velocity measurements  $v^{obs}$  with subscripts  $\alpha\beta$  ranging over longitude  $\phi$  and latitude  $\theta$ . The  $\bar{\epsilon}_{\phi\phi}$ ,  $\bar{\epsilon}_{\phi\theta}$ , and  $\bar{\epsilon}_{\theta\theta}$  are strain rate tensor components for each cell,  $S$  corresponds to the surface area of the related cell. The first double summation of the penalty function is the misfit to the observed GNSS velocity field subject to observational errors. The second double summation represents an a priori constraint to minimize strain. The weighting factor  $\nu$  determines the relative weight of velocity data and the minimal strain assumption in the penalty function, and thus the amount of smoothing in the interpolation.

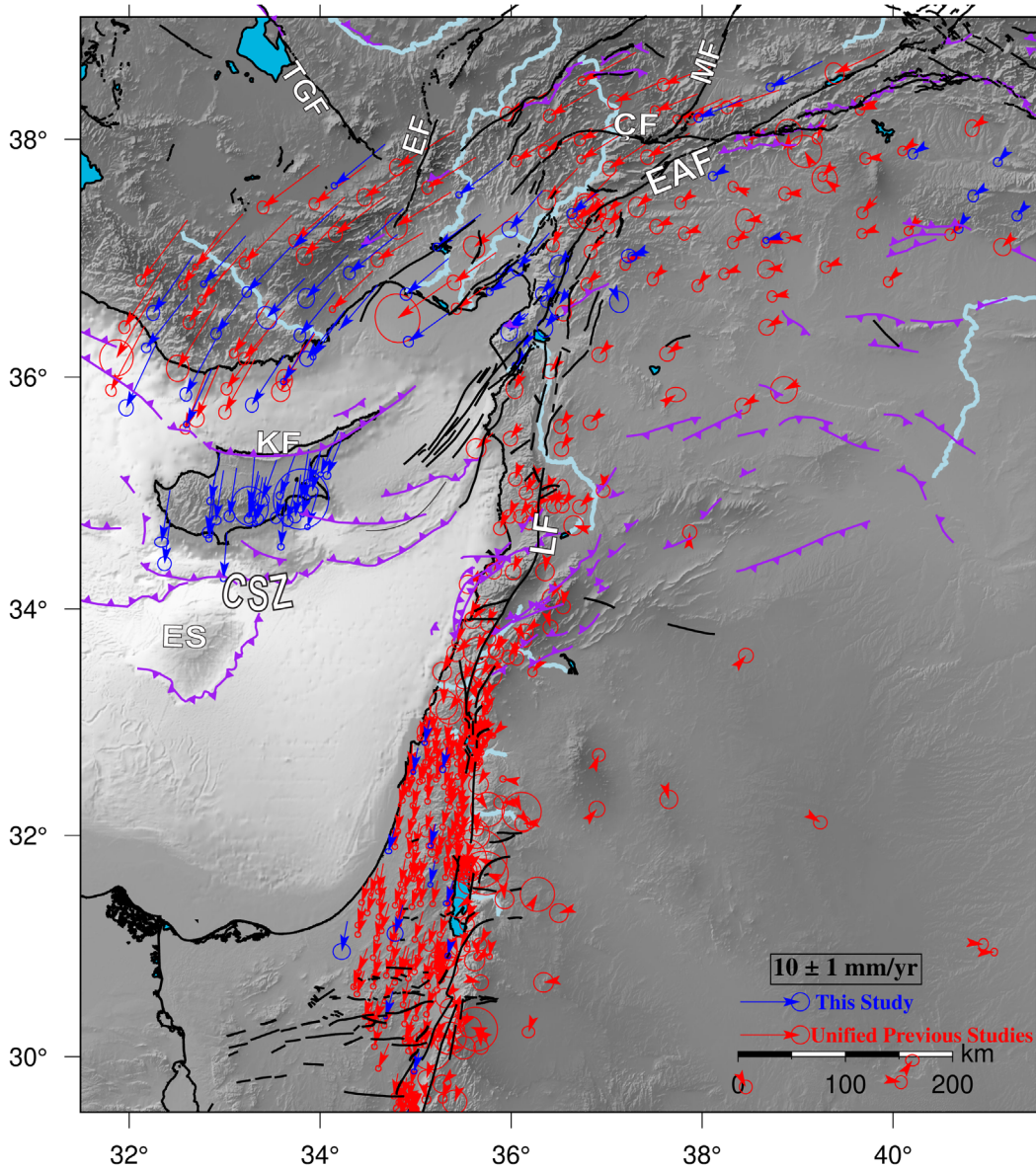


**Fig. 2.** Unified GNSS velocity field with respect to the fixed Arabian frame. Newly derived rates are depicted by blue arrows, while red arrows indicate rates from previous studies.

Here, we solely utilized the GNSS velocity field without imposing any plate motion boundary conditions. We also assigned a uniform  $\nu$  value to achieve the objective function. Experiments were made using lower  $\nu$  values in the grid cells in SW Cyprus and further offshore, where seismic catalogues show the clustering of earthquakes. If these are “damage” zones, their bulk deformability might be higher than other zones. However, these experiments did not significantly improve the fit to the GNSS velocities even in the near field sites in southern Cyprus justifying our decision not to include laterally varying  $\nu$  values.

Figure 3 shows the second invariant of the strain rate tensor (obeying the formula  $\sqrt{\dot{\epsilon}_{\varphi\varphi}^2 + \dot{\epsilon}_{\theta\theta}^2 + 2\dot{\epsilon}_{\varphi\theta}^2}$  where  $\dot{\epsilon}_{\varphi\varphi}$ ,  $\dot{\epsilon}_{\varphi\theta}$ , and  $\dot{\epsilon}_{\theta\theta}$  are the tensor components) overlain by the

seismicity of the region. The solution indicates, in general, low strain rates within Cyprus, where the second invariant rarely exceeds 20 nanostrain/yr. However, in Figure 4, deformation styles indicate a clear spatial variability of deformation in the island. A transpressive strike-slip regime is found along the Kyrenia range, while roughly N-S compression dominates in the southern part of the island (Fig. 4). On a larger scale, this strain partitioning within Cyprus seems to act as a diffuse transition that rotates the predominant compression from NW-SE in the Sinai block onto NE-SW in the Cilicia basin immediately to the north of Cyprus. Between Cyprus and Turkey, the shortening integrated along the principal strain rate axis between the coasts of Cyprus and Turkey amounts to a maximum of 0.8 mm/yr. The lack of GNSS data probably leads us to a strain rate field that is much smoother than reality in the

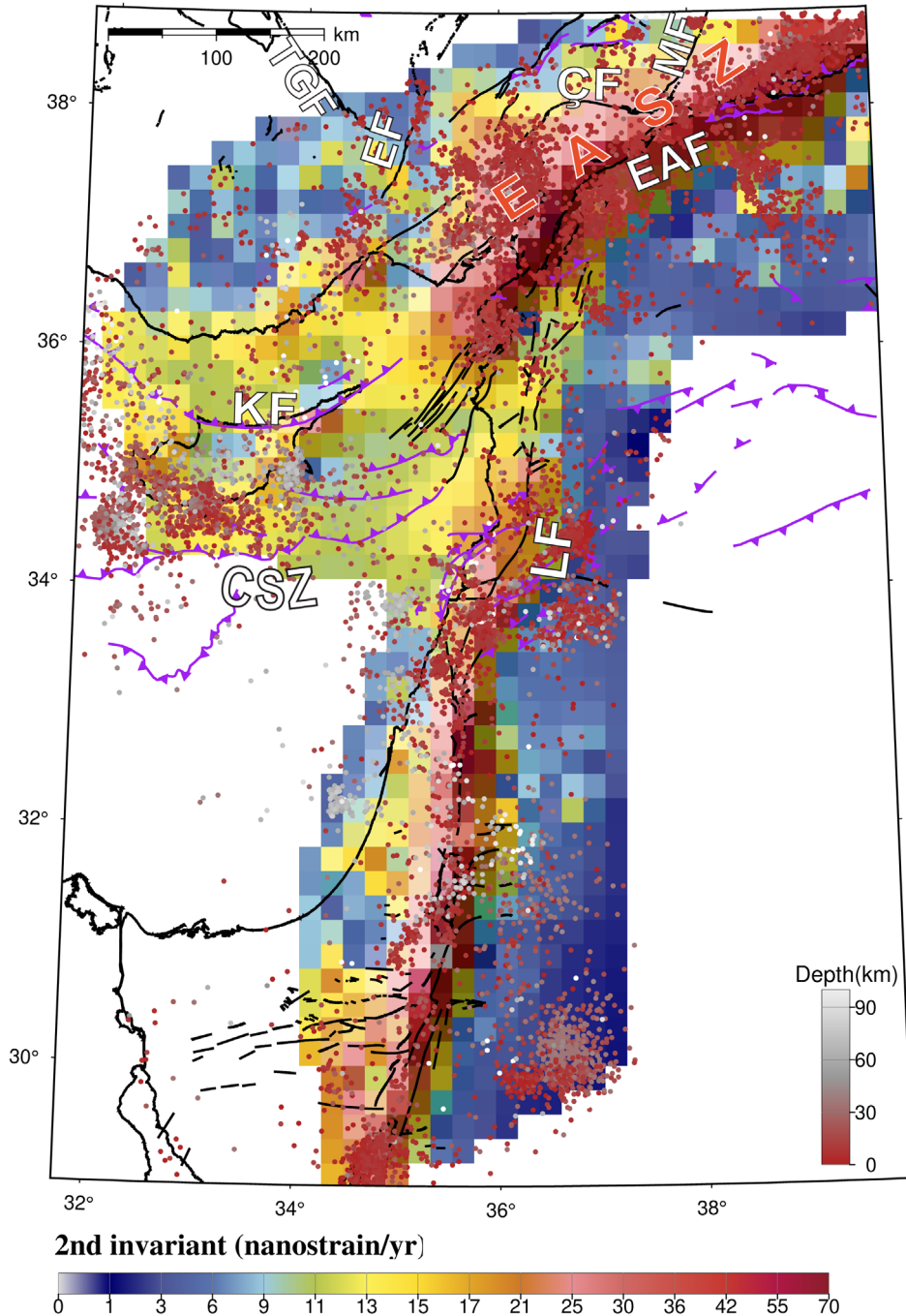


**Fig. 3.** Seismicity, colour-coded by depth, and the second invariant of the strain rate tensor. The seismicity catalogue was taken from (Kandilli *et al.*, 2001; <http://www.koeri.boun.edu.tr>). EASZ: East Anatolian Shear Zone.

Cilicia basin. Despite this, the solution shows a progressive transition from compression to strike-slip toward the NE, associated with a rotation of principle axes to N-S compression and E-W extension, eventually matching the dominant strain regime found on land in the Adana Basin.

A swath of higher strain rate (more than 30 nanostrain/yr) over a width of 50–60 km is found east of the Adana basin and extends NE along the northern side of the EAF, thus defining a broader East Anatolian shear zone (Fig. 3). The principal strain

directions (E-W extension and N-S compression) are consistent with left-lateral strike-slip motion. The areal strain ( $\dot{\epsilon}_{\varphi\varphi} + \dot{\epsilon}_{\theta\theta}$ ) is positive (see Fig. 4) except for at a few locations, indicating transtensive to extensional deformation, consistent with focal mechanisms (Fig. 3). Principal strain rate orientations retain the same orientation over a broader area, with lower strain rates, that include the Adana basin and the mountains north of it (Aladağlar, see Fig. 5). Areal strain indicates extension is dominant in these mountains while both

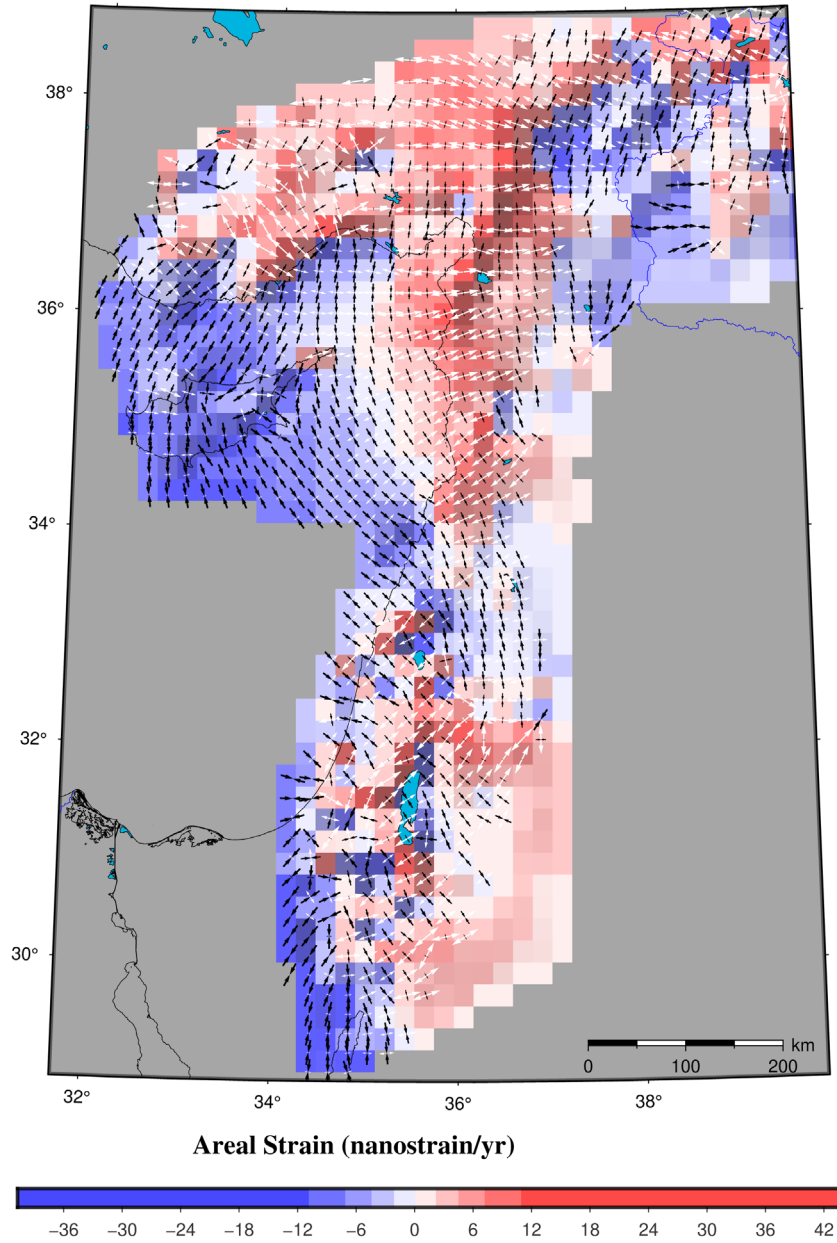


**Fig. 4.** Strain rate field of the area. Arrow crosses are the principal strain rate tensor components. The black arrow belongs to the compression component of each tensor while the white ones are the extensional component. Magnitudes of the principal rate crosses were normalized. The grid represents the areal strain change that accounts for the trace of the tensor for each cell (Blue means that the dominant force of the cell is compression, while red implies extension).

mildly transpressive and transtensive styles are found in the Adana basin. This may suggest that gravity influences strain distribution between topographic highs and the basin. The westward limit of this zone of E-W extension coincides with the Ecemiş Fault (see Fig. 4). This fault zone has taken up 60 km of left lateral slip since late Eocene and has been under transtension since Miocene (Sarıkaya *et al.*, 2015; Jaffey and Robertson, 2005; Umhoefer *et al.*, 2020; Yildirim *et al.*, 2016). The principal strain rate axes rotate to NE-SW compression and NW-SE extension west of the Ecemiş fault, which are respectively parallel and perpendicular to this part of the Taurus mountain range. The Ecemiş fault thus appears to

bound a zone of east-west extension related to the escape of the Anatolian plate. Strain rates within the Taurus range, west of the Ecemiş fault, are low (less than 10 nanostrain/year), and areal strain there is dominantly positive, but changes sign toward the coast in the south-western part of the range. This is the only part of Taurus where compressive strain is currently observed.

Along the Levant fault, the dominating principal strain orientations (see Fig. 4) are consistent with left-lateral shear on the fault. The GNSS coverage, however, provides poor kinematic constraints in the region from south of Turkey along the coast towards Israel and, in particular, along the east side of

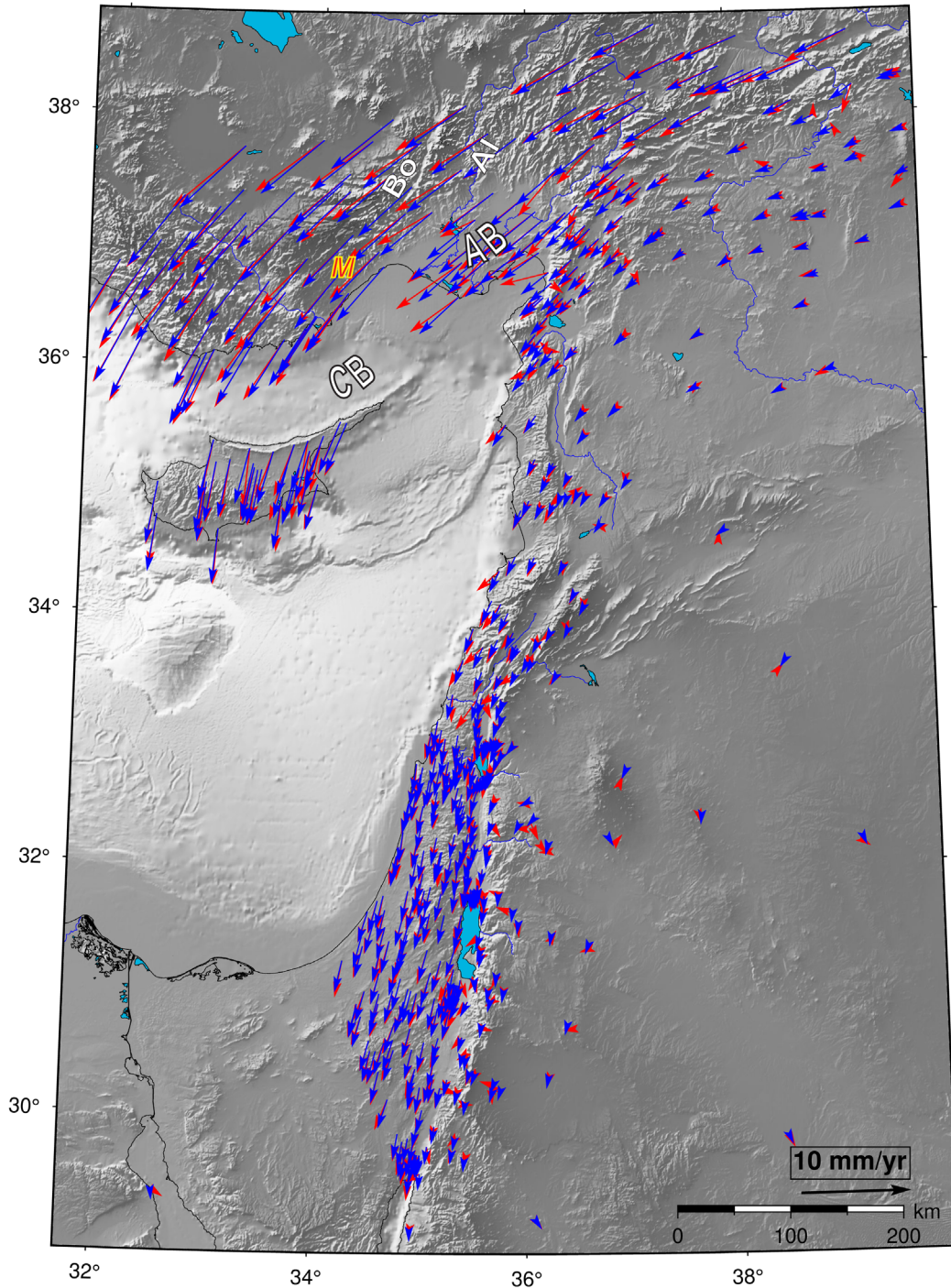


**Fig. 5.** Observed (red) and predicted (blue) GNSS velocities coming from continuum kinematic model inversion. Abbreviations: Bo: Bolkardğ, AI: Aladağlar.

the Levant fault where station coverage is sparse. Some short wavelength variability of the strain rate field, with compressional axes trending largely NW-SE, is evident within Israel, where the GNSS coverage is dense but mostly located on the western side of the Levant fault. The strain rates become less coherent towards the southern tip of Israel. North of Israel the zones of higher extension (positive areal strain) and compression (negative areal strain) do not match the location of the Lebanon restraining bend. This puzzling observation has

been reported previously (*cf.* Fig. 8 in [Gomez \*et al.\*, 2020](#)) and was possibly explained by the transfer of the compression onto offshore faults. Overall, zones of higher strain rate appear to roughly correlate with zones of higher seismic activity in the 0–30 km depth range corresponding to crustal seismicity ([Fig. 3](#)). We already mentioned that the recently ruptured segments of Çardak Fault and the EAF have been relatively silent before the earthquakes. On the other hand, the zone of E-W extension north of Karatas-Osmaniye Fault (KOF) and

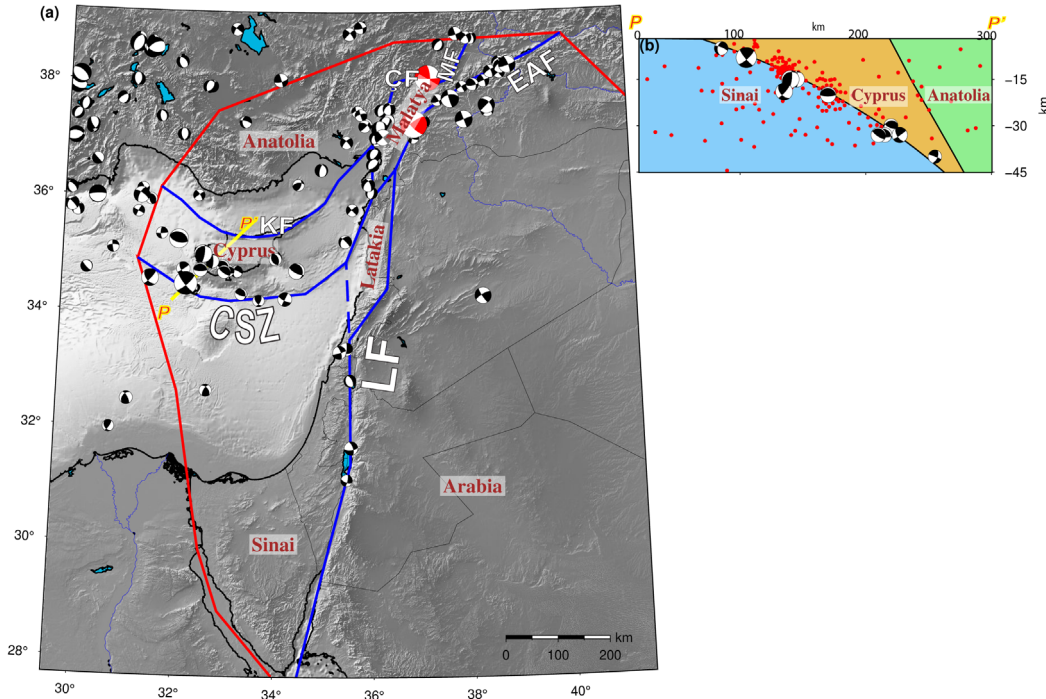


**Fig. 6.** (a) Block geometry and seismic activity around the region. Blue lines represent the boundaries defined as dislocation sources, red lines correspond to the other block boundaries which do not accumulate elastic strain. Focal mechanisms represent the earthquakes  $M_w 4.5$  between 1976-2022 (Ekström and Nettles, 1997) (the Feb 6 2023 earthquakes are highlighted in red). They were scaled according to their magnitudes. b) The cross-sectional view (marked as P-P' in the map) from the northern tip of the Cyprus Arc to the Kyrenia range (35 km width). Focal mechanisms (Ekström and Nettles, 1997) and red dots (Kandilli *et al.*, 2001; <http://www.koeri.boun.edu.tr>), which are the earthquakes that coincide with the domain of the cross-section, were projected onto the section.

east of Çardak Fault (CF) displays relatively high seismic activity. A cluster of seismic activity between Mersin and Bolkardağ also appears as a zone of relatively high strain rate in the GNSS interpolation with positive areal strain indicating extension (see Figs. 3 and 4). However, the orientation and style of the strain tensors determined in this area lack consistency and velocities present relatively higher interpolation residuals (Fig. 5). On the other hand, distributed compressive to transpressive deformation between northern Cyprus and the Anatolian coast may explain seismicity beneath the Cilicia basin. Clusters of seismic activity are also present within the Arabian plate and offshore Lebanon in zones of apparently low strain rates, but these areas on the edges of GNSS data coverage are not well constrained in the continuum model interpolation.

### 3.2 Block model

Our second modelling effort aims to determine the kinematic behaviour of the Nubia-Cyprus-Anatolia tectonic system in the context of an elastic block-based approach (McCaffrey *et al.*, 2007). Such a block model involves solving an inverse problem where the unknowns are Euler vectors for individual blocks, uniform strain rate tensor for each block, and coupling ratios on the fault node points. The model can, in principle, be constrained by GNSS velocities, geological fault slip rates and the azimuth of these rates, and earthquake focal mechanisms. Here we only used GNSS data.

The block geometry follows the main active fault zones (Levant fault, Cyprus Arc subduction, Kyrenia fault, East Anatolian fault), which are thought to be critical in shaping the regional tectonics (Fig. 6a). The distribution of seismicity is another key feature defining some block boundaries. The main differences in block architecture with previous studies result from the definition of a Cyprus block. On one hand, large-scale studies considered Cyprus to be a part of Anatolia and did not feature the Kyrenia range as a block boundary (Gomez *et al.*, 2020; Reilinger *et al.*, 2006). This is justifiable as it would not have been possible to constrain the motion of a Cyprus block with the very limited GNSS data available on the island at that time. On the other hand, a detailed kinematic study of the Hatay triple junction proposed connecting the Kyrenia arc to the EAF along the KOF (Özkan *et al.*, 2023) and this implies considering the area between Hatay and KOF as part of the Cyprus block. Inversion results obtained with this block geometry are presented in the appendix and we will show that this assumption results in large misfits. An alternate solution may be drawn taking into account a concentration of mostly extensional focal mechanisms along an N-S trend to the east of the Adana/Cilicia basin, 30 km west of the Levant fault. We assume this trend delineates a block boundary, separating Anatolia and the Cyprus block on its western side from a zone of complex deformation along the Levant and East Anatolian faults (the East Anatolian Shear Zone, Fig. 3). As internal block deformation is taken into account in the model (approximated as a uniform strain rate field in each block) this deforming zone can be defined as a block that stretches

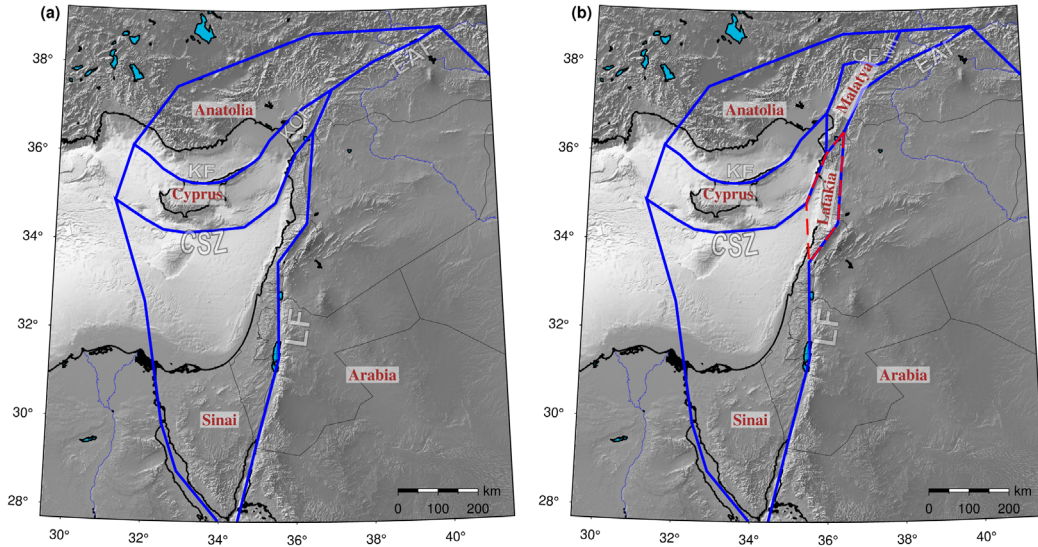


**Fig. 7.** Comparing Diverse Block Geometries: (a) This model adheres to the fault geometries proposed by (Özkan *et al.*, 2023) for Anatolia, without considering the Malatya block. (b) The blue solid lines delineate the block geometry consisting of five blocks (Model 2), while the red dashed line illustrates the inclusion of the Latakia block in Model 3, respecting the primary boundaries outlined in Model 2.

eastward along the East Anatolian fault toward Malatya (Klein *et al.*, 2022). Defining part of the northern boundary of this block along Çardak fault appears as an obvious hypothesis after the February 6 earthquakes. Moreover, Çardak (sometimes also called Sargu Fault) and Malatya faults (see Fig. 6a) are known to be active and have been included in previous tectonic models of the triple junction (Acarel *et al.*, 2019; Sançar *et al.*, 2019; Westaway, 2003).

To the south of Cyprus lies the Sinai block which is largely offshore. Its motion is crucial for the kinematics of the Cyprus Arc subduction but can only be constrained by velocities along the Levant coast and in the Sinai Peninsula. However, GNSS velocity fields in the Levant and in Southern Sinai do not fit in the same rigid block reference frame. Previous studies of Levant Fault kinematics proposed that the NE part of the Sinai microplate is fragmented in order to account for geodetic slip rates decreasing northward on the Levant fault (Gomez *et al.*, 2020). We thus consider an additional block, referred to as the “Latakia” block, to extend along the Levant coast (dashed blue line in Fig. 6a) north of Israel and compare solutions with and without this additional block. Note that (Gomez *et al.*, 2020) considers several blocks west of the Levant Fault. Hence, our Latakia block should be considered, like the Malatya block, as a deformable block. Moreover, south Sinai may be affected by extension around the Gulf of Aqaba but this extension cannot be well accounted for in our model, which simplifies the prolongation of the Levant fault into the Gulf of Aqaba as a vertical fault. We thus removed all GNSS rates south of 30° N for the south Sinai.

Along the block boundaries, we defined 5 main dislocation sources, capable of accumulating elastic deformation, on which the coupling ratio will be calculated by inversion (Fig. 6a). The Levant and East Anatolian faults, which obey nearly pure strike-slip motion, are modelled as

vertical planar sources. The boundary between the Anatolia and Malatya blocks is simplified as a vertical fault. However, to generate the geometry of dipping faults, such as the Cyprus subduction and Kyrenia fault, we followed published interpretations of seismic profiles (Aksu *et al.*, 2014a; Aksu *et al.*, 2005; Aksu *et al.*, 2021; Burton-Ferguson *et al.*, 2005; Calon *et al.*, 2005; Feld *et al.*, 2017; Hall *et al.*, (2005); Welford *et al.*, 2015). In addition, we utilized the seismicity of the region to compile earthquakes greater than  $M_w = 2.8$ . The earthquake locations validate the geometry of the main subduction seismogenic zone between Sinai and Cyprus down to a depth of 40 km but do not help define the geometry at the depth of Kyrenia fault between Cyprus and Anatolia (Fig. 6b).

We conducted a series of synthetic tests to determine the optimal spatial resolution of node points for the slip rate distribution, which was determined by the spatial coverage of the GNSS data along both strike and dip directions. To achieve this, we utilized a checkerboard test, in which we divided the main thrust interface south of Cyprus into planar cells, and monitored the level of recovery of the given slip rate boundary conditions using synthetic GNSS velocities at the same geographic locations as our data. We tested two different average cell sizes for the thrust interface: one with an average cell size of 35 km<sup>2</sup>, and the other with an average cell size of 10 km<sup>2</sup>. The tests were carried out without any synthetic observation noises. Our results indicated that the test conducted with larger patches had slightly better misfits than the one consisting of finer patch resolution. Figure S1 in the supplementary displays the checkerboard test solutions.

We evaluate inversion results using three different block geometries. It is crucial to emphasize that the models were inverted employing the same velocity field. In Model 1, we employed the geometry introduced by (Özkan *et al.*, 2023)

**Table 2.** Results of inversions for different inline models.  $\chi^2_v$  is the reduced chi-square ( $\chi^2$  divided by the number of Degrees of Freedom (DOF)).

Model Number	DOF	$\chi^2$	$\chi^2_v$
1	696	4219.25	6.06
2	662	1868.62	2.82
3	650	1761.52	2.71

around the triple junction. This model does not include a Malatya block between Anatolia and the East Anatolian Fault (EAF). Additionally, the Karata s-Osmaniye fault (see Fig. 7a) connects northeastward with the EAF, extending the boundary between Anatolia and Cyprus, and adding part of Hatay to the Cyprus block. Model 3 is the block model illustrated in Figure 6a. It includes a Latakia block in an attempt to account for the fragmentation of the Sinai plate (Gomez *et al.*, 2020). Model 2 is based on Model 3, without a Latakia block, the extent of which is here considered part of the Sinai plate. As indicated in Table 2, the residuals exhibit a substantial improvement in Models 2 and 3, which consider a Malatya block. This notable improvement is primarily attributed to larger misfits in Model 1 for stations in the Hatay region and Cyprus when these stations are forced to be part of the same block.

However, the improvement associated with the assumption of a Latakia block is subtle. Model 3 has a slightly lower misfit than Model 2 but with a small reduction of the chi-2 over the degree of freedom ratio (Tab. 2). An *F*-test, which is a powerful statistical method that allows us to assess whether the variability of the variances is significantly different, indicates this improvement is not significant (Tab. 2). Figures S2 and S3 in the supplementary show the first 2 model solutions.

Determining robust Euler pole parameters is of utmost importance for addressing the horizontal motion of the region. This problem is complicated by the fact that a large part of the Sinai plate is underwater and that the prolongation of the Sinai plate along the Levant coast (where GNSS stations are located) may be deforming. Euler poles of Sinai relative to Anatolia and to Arabia were obtained by the block model inversion. In order to estimate the Euler pole of the Nubia plate with respect to Anatolia we combined our determination of the Arabia-Anatolia pole with a Nubia-Arabia pole calculated in the ITRF No Net Rotation reference frame by (Altamimi *et al.*, 2017). The Nubia poles from this study, and (Reilinger *et al.*, 2006) are similar to each other, albeit with a slight difference in the rotation rates. The location of the Euler pole of (Reilinger *et al.*, 2006) for Sinai relative to Anatolia and ours are also close to each other. The rotation rate of the (Reilinger *et al.*, 2006) pole, however, is markedly faster resulting in a slower subduction velocity in our model. The data we used to constrain the motion of the Sinai block are essentially the same as in the previous studies, but we excluded data from South Sinai (below 30°N) as these cannot be fit in the same rigid reference frame, and this explains in large part the differences. The pole we determined provides a better fit of GNSS data along the Levant coast, but a worse fit of the GNSS data in the southern part of Sinai. We believe that this pole provides a

better description of the motion of the Mediterranean seafloor as it subducts beneath Cyprus (Tab. 3).

After an Euler pole and a uniform strain rate tensor are estimated for each block, a series of nonlinear inversions (*i.e.*, grid search and simulated annealing (Press *et al.*, 2007)) has been run iteratively to solve the coupling ratio on each node point. The Green's function that coincides with the location of the GNSS stations on the surface is determined with a rigorous approach to discretize the planar fault into rectangular patches (Okada, 1992). For the parametrization of fault coupling, we express the coupling ratio as constant between the surface and depth  $z_1$  (an inversion parameter at each node) and decaying exponentially below  $z_2$  where the fault starts fully slipping, as proposed by (Wang *et al.*, 2003).

Figure 8a represents the block motions along the boundaries defined as dislocation sources in Model 3. As the residuals we obtained are relatively small, we present histogram of both the north and east residuals in Figure 8b. On the Levant fault, the slip rate decreases steadily from south to north. It accommodates a  $4.7 \pm 0.6$  mm/yr slip rate from the Gulf of Aqaba to the Dead Sea with an almost purely left lateral strike-slip regime. At the Lebanese restraining bend, slip remains dominantly strike-slip at a  $3.0 \pm 6$  mm/yr rate, with a poorly constrained  $0.8 \pm 0.7$  mm/yr compressional rate. The Cyprus arc accommodates 3.5–6.2 mm/yr convergent rates reducing progressively from west to east. The motion of the Kyrenia fault, on the other hand, is mainly left lateral strike-slip from the northwesternmost tip to the east of the island with rates of 3.2–4.2 mm/yr. Although the slip rate along the western prolongation of the Kyrenia fault also obeys a left lateral strike-slip behaviour, the spatial distribution of our dataset may not be considered capable of resolving this particular region. Along the boundary between the Anatolian and Cyprus blocks on one side and the so-called Malatya block on the other side, the inversion indicates a significant  $\sim 1.3$  mm/yr extensional motion, which is in agreement with the predominantly extensional style of the earthquakes (see Fig. 6a). Meanwhile, there are relatively larger velocity residuals on the left side of the boundary, roughly coinciding with Adana Basin, that may represent active deformation not properly modelled with the assumed block geometry. Where the block boundary changes its azimuth from N-S to E-W and along the Çardak fault, the slip rate is an almost left lateral strike-slip behaviour with a  $2.0 \pm 1.0$  mm/yr rate. The Malatya fault, which extends from the eastern tip of the Çardak fault towards the north, has also left-lateral strike-slip motion accounting for  $1.7 \pm 1.2$  mm/yr. The motion on the East Anatolian fault zone, on the other hand, decreases from  $6.2 \pm 1.2$  to  $5.2 \pm 1$  mm/yr from the northernmost tip of the EAF to Kahramanmaraş triple junction where it connects with the Levant fault. Some additional shear is taken up by internal deformation of the Malatya block. Furthermore, the block motions for the two alternative model scenarios are provided in the supplementary document (Figs. S2 and S3).

Most block boundaries inverted for dislocation sources appear fully locked down the depth  $z_1$ . The only notable exception is the western part of the Kyrenia fault in Cyprus, but this result may not be reliable because of the distribution of velocity data, all located south of the fault with few points near the fault zones. The estimated  $z_1$  value for the Levant fault is consistently around 10 km. However, the inversion result

**Table 3.** Euler pole parameters estimated by this study and those from previous studies.

Plate Pair	Lat (°)	Lon (°)	$\Omega$ (°/Myr)	Reference
SIN-AN	31.77	37.91	-0.591	This study
SIN-AN	31.99	36.01	-1.185	Reilinger <i>et al.</i> (2006)
CY-AN	37.61	32.73	0.717	This study
NU-AN	31.67	34.83	-1.205	Reilinger <i>et al.</i> (2006)
NU-AN	31.69	34.88	-1.021	Altamimi <i>et al.</i> (2017)

indicates a depth of approximately 15 km (following the convention of (Wang *et al.*, 2003)) for  $z_2$  at the segments north of the Dead Sea, while it is 20 km at the segments south of it. For the EAF, the  $z_1$  value decreases from 20 to 13 km from south to north, while  $z_2$  remains relatively constant at 25 km. The locking behaviour of the Çardak fault is homogeneous along strike with  $z_1 = 8$  km and  $z_2 = 20$  km (see Fig. 9a). On the Cyprus arc subduction the inversion estimates a  $z_1$  value around 20–25 km depth, but due to the lack of GNSS data for the offshore part, the uncertainties of the coupling coefficient increase with the distance between the node points and Cyprus (Fig. 9b-c).

## 4 Discussion

We discuss our solutions and describe some implications of them including (1) the shear partitioning between the Cyprus subduction and Kyrenia fault; (2) the effect of this partitioning system around the East Anatolian shear zone toward the Kahramanmaraş triple junction; (3) a comparison of our solution with the previous studies around the Levant fault and the prolongation of distributed deformation for the northern part of the Levant fault; and (4) the results of our interseismic fault coupling model and coseismic slip behaviour of the 2023 Kahramanmaraş earthquakes.

### 4.1 Cyprus subduction, Kyrenia range and Taurus

The slip characteristics on both the Cyprus arc and Kyrenia range indicate that ongoing shear partitioning is the dominant regime for the area. The subduction is still active despite an incipient collision with the Eratosthenes seamount southwest of Cyprus, with near frontal convergence at a 6.0 mm/yr rate. The continuum deformation field (Fig. 4) obtained in and around the Taurus mountain range shows little shortening in the upper crust and, offshore, convergence between Taurus and Cyprus across the western part of the Cilicia basin is less than 1 mm/yr. The dominantly left-lateral strike-slip motion we find on the Kyrenia fault with a rate of 3.5–4.2 mm/yr, suggests a nearly perfect shear partitioning between the subduction and Kyrenia range. However, the distribution of seismicity in the area suggests the Kyrenia Fault may not be the only fault system involved. The Anatolia-Cyprus pole we calculated would also predict pure strike-slip relative motion on a fault running along the coast (the coast nearly follows a small circle for this pole) in the prolongation of The Kozan fault. This fault has been proposed to move at rates of 4–8 mm/yr based on sediment depocenter migration (Aksu *et al.*, 2014b). However, the GNSS residuals (although consistent in orientation with

left-lateral motion along the coast, see Fig. 5) are barely above noise level at about 1 mm/yr. Most probably, the strike-slip motion between Cyprus and Anatolia is dominantly taken up along the Kyrenia fault and its NE prolongation (the KOF).

The Euler poles published by previous studies (Gomez *et al.*, 2020; Reilinger *et al.*, 2006) only predict moderate obliquity on the Cyprus subduction, at about 20° south of Cyprus, which corresponds to the critical obliquity threshold for the onset shear partitioning above a subduction zone (McCaffrey, 1992). The rotation motion of Anatolia vs. Sinai and the arc shape of the subduction cause a lateral variation of obliquity so that 20° is a minimum value, but shear partitioning above subduction should not, in principle, lower slip vector obliquity below 15–20° (McCaffrey, 1992). It is thus possible that forces applied on the E and W boundaries of the Cyprus block play a role. The Cyprus block interacts with the Malatya block at its NE end and kinematic conditions on this boundary are extensional. It is thus possible that the forces applied in this zone near the triple junction influence the motion of the Cyprus block and particularly the amount of strike-slip taken up by the Kyrenia fault.

The fault coupling model of the Cyprus arc subduction is characterized by full locking from the surface to 20 km, which is consistent with (Feld *et al.*, 2017; Welford *et al.*, 2015), transitioning to partial locking between 20 and 30 km. The seismic activity during the instrumental period aligns with our coupling model, with the majority of earthquakes occurring within the 12–20 km depth range of the Cyprus subduction zone (see Fig. 6b). Conversely, the Kyrenia fault exhibits a distribution of locking extending from 0 to 7 km, transitioning to freely slipping behaviour beyond that depth. However, seismic activity on this fault is too low to provide an independent constraint on the depth range of the seismogenic zone.

### 4.2 East Anatolian shear zone

In the vicinity of the triple junction the shear between Anatolia and Arabia is distributed over a zone that we defined as a block (the Malatya block). On the East Anatolian fault, we obtain 5.1–6.2 mm/yr strike-slip rates that are lower than most previous studies (Reilinger *et al.*, 2006). However, analyses of a high-resolution velocity field obtained by combining GNSS and InSAR data (Weiss *et al.*, 2020) found a laterally varying interseismic loading rate on the EAF (Güvercin *et al.*, 2022; Li *et al.*, 2023). The strike-slip rate on the Malatya fault we obtained (1.7 mm/yr) is consistent with previous studies (2013). The strike-slip rate on the Çardak fault we obtained from the block model is 1.8 mm/yr and is comparable with a 2 mm/yr slip rate calculated from geomorphological offsets

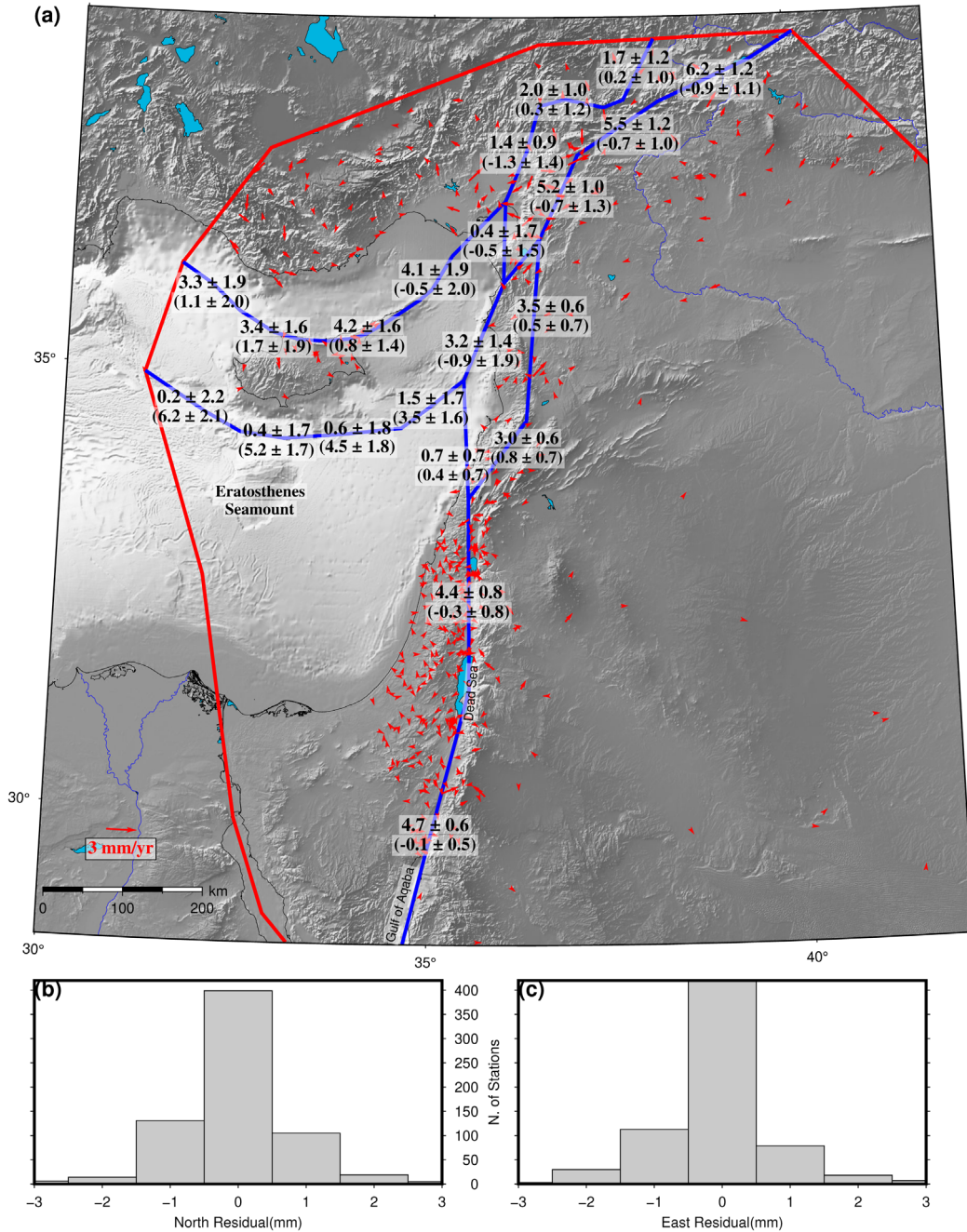


**Fig. 8.** (a) Block motions and residual velocities. The values with no parentheses are the strike-slip rates (Positive means left lateral) and the slip rates within the parentheses are convergence rates (positive means compression). The red arrows are the residual velocities coming from model 3 (best-fitting model). (b) and (c) Panels show the histogram view of the north and east velocity components residuals.

(Westaway, 2003). In addition, the principal strain rate orientations between these two faults indicate left-lateral shear co-linear with shear along the East Anatolian fault zone (see Figs. 8 and 4) with an average rate of 35 nanostrain per year and a small extensional component (Fig. 3). Assuming simple shear, the internal deformation of the Malatya block over an average width of 50 km amounts to about 1.7 mm/yr. The strike-slip motion between Anatolia and Arabia thus appears to be distributed between the East Anatolian fault, the faults defining the northern boundary of the Malatya block and

the internal deformation of the block. These three components add up to 8.5–9.7 mm/yr, which is consistent with previous estimations of Arabia/Anatolia plate motion (Bletery *et al.*, 2020; Reilinger *et al.*, 2006). The block boundaries we propose differ from the geometry proposed by (Özkan *et al.*, 2023) in that they connect the Karataş-Osmaniye fault to the EAF near Kahramanmaraş and thus do not allow shear partitioning east of the triple junction. Their geometry cannot account for the loading of Çardak Fault which was ruptured during the second earthquake of the February 6, 2023, earthquake doublet

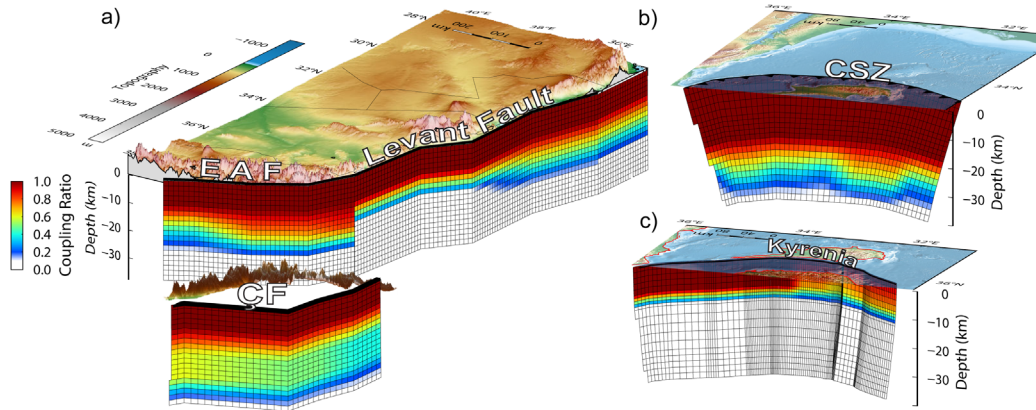


**Fig. 9.** The locking distribution on the dislocation sources within the block model. (a) Levant, East Anatolian, and Çardak Faults (and the prolongation of the northwestern boundary of the Malatya block), (b) Cyprus Subduction Zone, and (c) Kyrenia fault.

(Barbot *et al.*, 2023; Toda *et al.*, 2023). Our solution with an N-S transtensional boundary connecting to Çardak fault has a lower misfit and also better represents mapped active faults (Emre *et al.*, 2018; Fig. 1b). We conclude that part of the EAF motion is partitioned from the main fault in a broader zone around the triple junction, resulting in decreased interseismic loading rates on the main strand of the EAF.

#### 4.3 Levant fault zone

Block-based model inversion indicates that the Levant fault accommodates a 3.5–4.7 mm/yr slip rate, and it decreases slightly but steadily from south to north. This result is consistent with previous studies such as (Al Tarazi *et al.*, 2011; Gomez *et al.*, 2020; Hamiel and Piatibratova, 2021; Li *et al.*, 2024; Sadeh *et al.*, 2012). Gomez *et al.* (2020) found a decreasing motion northward from 5.0 mm/yr to  $2.2 \pm 0.5$  mm/yr as they consider two block boundaries transferring part of the Levant fault motion to hypothetical offshore structures. Our inversion results find less transfer of motion to offshore faults. For instance, only  $0.7 \pm 0.7$  mm/yr are transferred to the western boundary of the Latakia block compared to  $1.5 \pm 0.5$  mm/yr for the corresponding block boundary in (Gomez *et al.*, 2020). However, uncertainties are large so that inversion results remain compatible. Several factors may contribute to a lower velocity on the offshore block boundary and a higher uncertainty in our results. Our data set is different and possibly with a higher noise level as it combines several different studies, a different inversion code is used that allows internal block deformation, and block boundaries also differ.

#### 4.4 Interseismic fault coupling model and 2023 Kahramanmaraş earthquake doublet

During the Feb 6, 2023 sequence, ruptures occurred on the southern and northern boundaries of Malatya block. The main shock (Mw 7.8) occurred on the East Anatolian and Levant faults while the large Mw 7.6 aftershock occurred on Çardak Fault (CF), corresponding to a moment magnitude about half of that of the main shock (Hussain *et al.*, 2023; Toda *et al.*, 2023). The occurrence of these events shows that both boundaries are seismically active and present a high seismic

hazard. Our interseismic coupling inversion results find both faults are fully and homogeneously locked down to at least 10 km depth, but we cannot exclude that heterogeneities may be present but not resolvable with the GNSS data set we used. Based on InSAR and seismicity distributions, previous studies found shallow locking depth and aseismic creep on the EAF east of E038.5° longitude (Bletery *et al.*, 2020; Cakir *et al.*, 2023; Konca *et al.*, 2021). Moreover, the depth of locking near the bend between EAF and Levant Fault (Fig. 9a) may be overestimated because of the simplified geometry of the block boundary where two faults branches are in fact present (the Nurdai-Pazarck Fault and the Pazarck segment of the EAF). Several research groups worked on the coseismic slip distributions on both EAF and CF using seismological records, SAR interferometry, optical (Sentinel-2) images, and coseismic GNSS data and various inversions and joint inversions have been published using these data (Barbot *et al.*, 2023; Chen and Zhou, 2024; Jia *et al.*, 2023; Li *et al.*, 2023; Melgar *et al.*, 2023; Toda and Stein, 2024). The average distribution of coseismic slip with depth is consistent with a locking depth of 10–15 km for both faults with a progressive transition down to 20 km (Jia *et al.*, 2023). These coseismic slip models also find that the smaller earthquake has, in fact, larger displacements but over a smaller rupture length. This implies, taking into account interseismic loading rates, that the recurrence interval is very different on these two faults. Estimates of surface displacement from Sentinel-2 image correlation are 4 m on average over a large part of the main shock rupture with a local maximum of about 7 m and 6 m on average for the aftershock with a maximum of 8–9 m (Barbot *et al.*, 2023; Hussain *et al.*, 2023). Using our interseismic backslip estimates, recurrence intervals of 750 to 1500 years are inferred for the East Anatolian Fault and from 3000 to 5000 years on the Çardak Fault. It thus appears that triggering of the Çardak Fault does not occur each time a large earthquake occurs on the East Anatolian Fault, and probably does so less than once every three cycles on the EAF. Moreover, the Mw 7.8 earthquake is a multi-segment rupture (Barbot *et al.*, 2023), and such events have longer recurrence intervals than those estimated for characteristic earthquakes on individual segments. Estimates from single segments range from 100 years to about 900 years along the East Anatolian Fault with the longest intervals and largest maximum magnitude (Mw 7.4) in the Kahramanmaraş

triple junction area (Güvercin *et al.*, 2022). It is important to note that that study took into account a westward decrease of interseismic loading rates along the EAF segments. The duration of seismic cycles involving a multi-segment rupture is even longer. Their estimation depends on complex scenarios that combine multi-segment and single-segment ruptures and ranges from 700 to 2500 years (Karabulut *et al.*, 2023). We conclude that shear partitioning in the Kahramanmaraş triple junction is one of the factors contributing to very long earthquake cycles on the EAF. Moreover, the earthquake hazard on secondary faults must not be ignored even though large events on these slower faults may have even longer recurrence intervals.

## 5 Conclusion

Acquisition of new GNSS data on Cyprus and southern Turkey brings new insight into the deformation of the region around the Kahramanmaraş triple junction. It shows that the present-day deformation of Cyprus may be understood as a shear partitioning system between the Cyprus arc subduction and the Kyrenia fault, which appears to be a dominantly strike-slip boundary. Thus, the incipient collision with the Eratosthenes Seamount may not have yet perturbed much the kinematics of the Cyprus subduction. On the other hand, the northeast continuation of the shear partitioning system toward the Anatolia/Arabia collision zone brings further complexity to the Kahramanmaraş triple junction.

In the Anatolia-Arabia plate boundary, our study demonstrates that part of the motion on the East Anatolian Fault is distributed away from the main fault in the vicinity of the triple junction, as was previously shown for the Levant fault in the Arabia-Nubia plate boundary (Gomez *et al.*, 2020). Thus, the EAF is not the only deformation source in the East Anatolian shear zone as deformation is also distributed on secondary faults such as Çardak and Malatya faults. The earthquake sequence that occurred on February 6 2023 emphasizes the earthquake hazard presented by secondary faults in complex plate boundary zones. In the study area, the kinematics of faults offshore of the Levant and Hatay coasts still need consideration. On land, the slip rates calculated on the faults bounding the Malatya block result in very long earthquake cycles of 750-2000 years for the part of the EAF that ruptured recently and probably 3000-5000 years for Çardak Fault. How such rare events may be considered in hazard assessment poses questions.

## Acknowledgments

We thank our editors and reviewers whose constructive feedback and thoughtful suggestions have significantly improved this manuscript. We want to thank the T.C. Ministry of Defence General Directorate of Mapping for their contribution during the field studies and for sharing previous GNSS observations they measured. We are grateful to Ali Fahri Özten and Sebat Proje ve Mühendislik for the instrument supply and accommodation in Cyprus. We also want to thank Fatih Taskran, Mert Topal, Mustafa Ozan Güldoğan and Dr Ali İhsan Kurt for their priceless effort during the field observations. Dr. Robert McCaffrey's remarks, especially in establishing the block model, guided us. We also thank Xavier Le Pichon and Solène Antoine for their comments and discussions on understanding the

recent earthquakes. This study was funded by the Istanbul Technical University Scientific Research Projects Coordination Unit with an MGA-2020-42584 ID Number research project. Moreover, it is part of the Ph.D. thesis of the corresponding author. The modeling part was carried out mostly at Centre Européen de Recherche et d'Enseignement des Géosciences de l'Environnement (CEREGE) in the scope of the TUBITAK 2214A International Research Scholarship during Ph.D. for Ph.D. candidates program with the project number 1059B142000638. The calculation of daily coordinates of GNSS sites reported in this paper was performed at TUBITAK ULAKBIM, High Performance and Grid Computing Center (TRUBA resources).

## Supplementary material

**Table S1:** GNSS velocities (horizontal components) of newly derived rates with respect to both the Arabian and ITRF14 fixed reference frame.

**Table S2:** Life span of survey mode GNSS sites.

**Table S3:** Helmert Transformation Parameters of each rotation.

**Table S4:** Unified GNSS velocities (horizontal components) coming from previously published rates with respect to both the Arabian and ITRF14 fixed reference frame.

**Fig. S1:** Checkerboard Test Solution.

**Fig. S2:** Block Model Comparison - 1st Model outcomes.

**Fig. S3:** Block Model Comparison - 2nd Model outcomes.

The Supplementary Material is available at <https://www.bsgf.fr/10.1051/bsgf/2024012/olm>.

## References

- Acarel D, Cambaz MD, Turhan F, Mutlu AK, Polat R. 2019. Seismotectonics of Malatya Fault, Eastern Turkey. *Open Geosci* 11: 1098–1111
- Aksu A, Calon T, Hall J, Kurtboğan B, Gürçay S, Çifçi G. 2014a. Complex interactions fault fans developed in a strike-slip system: Kozan Fault Zone, Eastern Mediterranean Sea. *Marine Geol* 351: 91–107.
- Aksu A, Calon T, Hall J, Mansfield S, Yasar D. 2005. The Cilicia–Adana basin complex, Eastern Mediterranean: neogene evolution of an active fore-arc basin in an obliquely convergent margin. *Mar Geol* 221: 121–159.
- Aksu A, Hall J, Yaltrak C. 2021. Miocene–Quaternary tectonic, kinematic and sedimentary evolution of the eastern Mediterranean Sea: a regional synthesis. *Earth-Science Rev* 220: 103719.
- Aksu A, Walsh-Kennedy S, Hall J, Hiscott R, Yaltrak C, Akhun S, Çifçi G. 2014b. The Pliocene–Quaternary tectonic evolution of the Cilicia and Adana basins, eastern Mediterranean: special reference to the development of the Kozan Fault zone. *Tectonophysics* 622: 22–43.
- Al Tarazi E, Abu Rajab J, Gomez F, Cochran W, Jaafar R, Ferry M. 2011. GPS measurements of near-field deformation along the southern Dead Sea Fault System. *Geochem Geophys Geosyst* 12: <https://doi.org/10.1029/2011GC003736>
- Alchalbi A, Daoud M, Gomez F, McClusky S, Reilinger R, Romeyeh MA, Alsoud A, Yassminh R, Ballani B, Darawcheh R, Sbeinati R,

- Radwan Y, Masri RA, Bayerly M, Ghazzi RA, Barazangi M. 2010. Crustal deformation in northwestern Arabia from GPS measurements in Syria: slow slip rate along the northern Dead Sea Fault. *Geophys J Int* 180: 125–135.
- Altamimi Z, Métivier L, Rebischung P, Rouby H, Collilieux X. 2017. ITRF2014 plate motion model. *Geophys J Int* 209: 1906–1912.
- Altamimi Z, Rebischung P, Métivier L, Collilieux X. 2016. Itrf2014: a new release of the international terrestrial reference frame modeling nonlinear station motions. *J Geophys Res: Solid Earth* 121: 6109–6131.
- Barbot S, Luo H, Wang T, Hamiel Y, Piatibratova O, Javed MT, Braitenberg C, Gurbuz G. 2023. Slip distribution of the February 6, 2023 Mw 7.8 and Mw 7.6, Kahramanmara, Turkey earthquake sequence in the East Anatolian Fault Zone. *Seismica* 2: <https://seismica.library.mcgill.ca/article/view/502>.
- Bletery Q, Cavalíé O, Nocquet JM, Ragon T. 2020. Distribution of interseismic coupling along the North and East Anatolian faults inferred from InSAR and GPS data. *Geophys Res Lett* 47: e2020GL087775.
- Boehm J, Werl B, Schuh H. 2006. Troposphere mapping functions for GPS and very long baseline interferometry from European Centre for Medium-Range Weather Forecasts operational analysis data. *J Geophys Res: Solid Earth* 111: <https://doi.org/10.1029/2005JB003629>.
- Brun JP, Faccenna C, Gueydan F, Sokoutis D, Philippon M, Kydonakis K, Gorini C. 2016. The two-stage Aegean extension, from localized to distributed, a result of slab rollback acceleration. *Can J Earth Sci* 53: 1142–1157.
- Burton-Ferguson R, Aksu A, Calon T, Hall J. 2005. Seismic stratigraphy and structural evolution of the Adana Basin, eastern Mediterranean. *Mar Geol* 221: 189–222.
- Çakir Z, Doğan U, Akoğlu AM, Ergintav S, Özarpaç S, Özdemir A, Nozadkhalil T, Çakir N, Zabcı C, Erkoç MH, Basmenji M, Köküm M, Bilham R. 2023. Arrest of the mw 6.8 january 24, 2020 Elazığ (Turkey) earthquake by shallow fault creep. *Earth Planet Sci Lett* 608: 118085.
- Calon T, Aksu A, Hall J. 2005. The Neogene evolution of the outer Latakia Basin and its extension into the eastern Mesoarea Basin (Cyprus), eastern Mediterranean. *Mar Geol* 221: 61–94.
- Cavalíé O, Jónsson S. 2014. Block-like plate movements in eastern Anatolia observed by InSAR. *Geophys Res Lett* 41: 26–31.
- Chen J, Zhou Y. 2024. Coseismic slip distribution of the 2023 earthquake doublet in Turkey and Syria from joint inversion of Sentinel-1 and Sentinel-2 data: an iterative modelling method for mapping large earthquake deformation. *Geophys J Int* 237: 636–648.
- Eckström G, Nettles M. 1997. Calibration of the HGLP seismograph network and centroid-moment tensor analysis of significant earthquakes of 1976. *Phys Earth Planetary Interiors* 101: 219–243.
- Emre Ö, Duman T, Özalp S, Elmac H, Olun S, Saroglu F. 2013. Active fault map of Turkey with explanatory text. General Directorate of Mineral Research and Exploration Special Publication Series 30.
- Emre Ö, Duman TY, Özalp S, Sarolu F, Olun S, Elmac H, Can T. 2018. Active fault database of Turkey. *Bull Earthquake Eng* 16: 3229–3275.
- England P, Houseman G, Nocquet JM. 2016. Constraints from GPS measurements on the dynamics of deformation in Anatolia and the Aegean. *J Geophys Res: Solid Earth* 121: 8888–8916.
- Feld C, Mechie J, Hübscher C, Hall J, Nicolaides S, Gurbuz C, Bauer K, Loudon K, Weber M. 2017. Crustal structure of the Eratosthenes Seamount, Cyprus and S. Turkey from an amphibian wide-angle seismic profile. *Tectonophysics* 700-701: 32–59.
- Gomez F, Cochran WJ, Yassminh R, Jaafar R, Reilinger R, Floyd M, King RW, Barazangi M. 2020. Fragmentation of the Sinai Plate indicated by spatial variation in present-day slip rate along the Dead Sea Fault System. *Geophys J Int* 221: 1913–1940.
- Gomez F, Karam G, Khawlie M, McClusky S, Vernant P, Reilinger R, Jaafar R, Tabet C, Khair K, Barazangi M. 2007. Global Positioning System measurements of strain accumulation and slip transfer through the restraining bend along the Dead Sea fault system in Lebanon. *Geophys J Int* 168: 1021–1028.
- Güvercin SE, Karabulut H, Konca AO, Doğan U, Ergintav S. 2022. Active seismotectonics of the East Anatolian Fault. *Geophys J Int* 230: 50–69.
- Haines AJ, Holt WE. 1993. A procedure for obtaining the complete horizontal motions within zones of distributed deformation from the inversion of strain rate data. *J Geophys Res* 98.
- Hall J, Calon T, Aksu A, Meade S. 2005. Structural evolution of the Latakia Ridge and Cyprus Basin at the front of the Cyprus Arc, eastern Mediterranean Sea. *Mar Geol* 221: 261–297.
- Hamiel Y, Piatibratova O. 2021. Spatial variations of slip and creep rates along the southern and central dead sea fault and the Carmel–Gilboa Fault System. *J Geophys Res: Solid Earth* 126: e2020JB021585.
- Herring TA, King RW, Floyd MA, McClusky SC. 2018a. Introduction to GAMIT/GLOBK, Release 10.7, GAMIT/GLOBK Documentation.
- Herring TA, King RW, Floyd MA, McClusky SC. 2018b. GLOBK Reference Manual Global Kalman filter VLBI and GPS analysis program Release 10.7. Massachusetts Institute of Technological, Cambridge, Massachusetts.
- Herring TA, Davis JL, Shapiro II. 1990. Geodesy by radio interferometry: The application of Kalman filtering to the analysis of very long baseline interferometry data. *J Geophys Res: Solid Earth* 95: 12561–12581.
- Hussain E, Kalaycıoğlu S, Milliner CW, Çakir Z. 2023. Preconditioning of the 2023 Kahramanmaraş (Türkiye) earthquake disaster. *Nat Rev Earth Environ* 5–7.
- Jaffey N, Robertson A. 2005. Non-marine sedimentation associated with Oligocene–Recent exhumation and uplift of the Central Taurus Mountains, S Turkey. *Sediment Geol* 173: 53–89.
- Jia Z, Jin Z, Marchandon M, Ulrich T, Gabriel AA, Fan W, Shearer P, Zou X, Rekoske J, Bulut F, Garagon A, Fialko Y. 2023. The complex dynamics of the 2023 kahramanmaraş, turkey, m<sub>w</sub> 7.8-7.7 earthquake doublet. *Science* 381: 985–990.
- Karabulut H, Güvercin SE, Hollingsworth J, Konca AO. 2023. Long silence on the East Anatolian Fault Zone (Southern Turkey) ends with devastating double earthquakes (6 February 2023) over a seismic gap: implications for the seismic potential in the Eastern Mediterranean region. *J Geol Soc* 180: <https://doi.org/10.1144/jgs2023-021>.
- Karig DE, Kozlu H. 1990. Late Palaeogene–Neogene evolution of the triple junction region near Maraş, south-central Turkey. *J Geol Soc* 147: 1023–1034.
- Kandilli O, Earthquake RI, Boğaziçi U. 2001. Kandilli Observatory And Earthquake Research Institute (KOERI), *International Federation of Digital Seismograph Networks*, <https://www.fdsn.org/networks/detail/KO/>
- Klein EC, Özbey V, Ozeren MS, Sengör AM, Haines AJ, Henry P, Tar E, Zabcı C. 2022. New gnss observations in cyprus and block and

- continuum models for eastern mediterranean, in: *AGU Fall Meeting Abstracts*, pp. G35B–0326.
- Konca AO, Karabulut H, Güvercin SE, Eskiköy F, Özarpacı S, Özdemir A, Floyd M, Ergintav S, Doğan U. 2021. From interseismic deformation with near-repeating earthquakes to coseismic rupture: a unified view of the 2020 mw6.8 sivrice (elazığ) eastern Turkey earthquake. *J Geophys Res: Solid Earth* 126: e2021JB021830.
- Kandilli O, Earthquake RI, Boğaziçi U. 2001. Kandilli Observatory And Earthquake Research Institute (KOERI), *International Federation of Digital Seismograph Networks*, <https://www.fdsn.org/networks/detail/KO/>
- Kurt IA, Özbakir DA, Cingoz A, Ergintav S, Dogan U, Özarpacı S. 2022. Contemporary velocity field for Turkey inferred from combination of a dense network of long term GNSS observations. *Turk J Earth Sci* <https://doi.org/10.55730/yer-2203-13>.
- Le Beon M, Klinger Y, Amrat AQ, Agnon A, Dorbath L, Baer G, Ruegg JC, Charade O, Mayyas O. 2008. Slip rate and locking depth from GPS profiles across the southern Dead Sea Transform. *J Geophys Res: Solid Earth* 113.
- Le Pichon X, Francheteau J. 1978. A plate-tectonic analysis of the Red Sea—Gulf of Aden Area. *Tectonophysics* 46: 369–406.
- Le Pichon X, Gaulier JM. 1988. The rotation of Arabia and the Levant fault system. *Tectonophysics* 153: 271–294.
- Le Pichon X, Kreemer C. 2010. The Miocene-to-present kinematic evolution of the eastern mediterranean and middle east and its implications for dynamics. *Annu Rev Earth Planetary Sci* 38: 323–351.
- Le Pichon X, Sengör AC, Imren C. 2019. A new approach to the opening of the eastern Mediterranean Sea and the origin of the Hellenic subduction zone. Part 2: The Hellenic subduction zone. *Can J Earth Sci* 56: 1144–1162.
- Li S, Wang X, Tao T, Zhu Y, Qu X, Li Z, Huang J, Song S. 2023. Source model of the 2023 Turkey earthquake sequence imaged by sentinel-1 and GPS measurements: implications for heterogeneous fault behavior along the East Anatolian Fault Zone. *Remote Sens* 15.
- Li X, Jónsson S, Liu S, Ma Z, Castro-Perdomo N, Cesca S, Masson F, Klinger Y. 2024. Resolving the slip-rate inconsistency of the northern dead sea fault. *Sci Adv* 10: eadj8408.
- Mahmoud S, Reilinger R, McClusky S, Vernant P, Tealeb A. 2005. GPS evidence for northward motion of the Sinai Block: implications for E. Mediterranean tectonics. *Earth Planetary Sci Lett* 238: 217–224.
- Mahmoud Y, Masson F, Meghraoui M, Cakir Z, Alchalbi A, Yavasoglu H, Yönlü O, Daoud M, Ergintav S, Inan S. 2013. Kinematic study at the junction of the East Anatolian fault and the Dead Sea fault from GPS measurements. *J Geodyn* 67: 30–39.
- McCaffrey R. 1992. Oblique plate convergence, slip vectors, and forearc deformation. *J Geophys Res: Solid Earth* 97: 8905–8915.
- McCaffrey R, Qamar AI, King RW, Wells R, Khazaradze G, Williams CA, Stevens CW, Vollick JJ, Zwick PC. 2007. Fault locking, block rotation and crustal deformation in the Pacific Northwest. *Geophys J Int* 169: 1315–1340.
- McKenzie D. 1972. Active tectonics of the Mediterranean region. *Geophys J Int* 30: 109–185.
- McKenzie D. 1976. The East Anatolian Fault: A major structure in Eastern Turkey. *Earth Planet Sci Lett* 29: 189–193.
- McKenzie D, Davies D, Molnar P. 1970. Plate tectonics of the Red Sea and east Africa. *Nature* 226: 243–248.
- Melgar D, Taymaz T, Ganas A, Crowell BW, Öcalan T, Kahraman M, Tsironi V, Yolsal-Çevikbil S, Valkaniotis S, Irmak TS, *et al.* 2023. Sub-and super-shear ruptures during the 2023 Mw 7.8 and Mw 7.6 earthquake doublet in SE Türkiye. *Seismica* 2: [10.26443/seismica.v2i3.387](https://doi.org/10.26443/seismica.v2i3.387).
- Okada Y. 1992. Internal deformation due to shear and tensile faults in a half-space. *Bull Seismolog Soc Am* 82: 1018–1040.
- Özbey V, Özeren MS, Henry P, Klein E, Galgana G, Karabulut H, Lange D, McCaffrey R. 2021. Kinematics of the Marmara Region: a fusion of continuum and block models. *Mediterranean Geosci Rev* 3: 57–78.
- Özeren MS, Holt WE. 2010. The dynamics of the eastern Mediterranean and eastern Turkey. *Geophys J Int* 183: 1165–1184.
- Reilinger R, McClusky S, Vernant P, Lawrence S, Ergintav S, Cakmak R, Ozener H, Kadirov F, Guliev I, Stepanyan R, Nadariya M, Hahubia G, Mahmoud S, Sakr K, ArRajehi A, Paradissis D, Al-Aydrus A, Prilepin M, Guseva T, Evren E, Dmitrotsa A, Filikov SV, Gomez F, Al-Ghazzi R, Karam G. 2006. GPS constraints on continental deformation in the Africa-Arabia-Eurasia continental collision zone and implications for the dynamics of plate interactions. *J Geophys Res: Solid Earth* 111: 1–26.
- Sadeh M, Hamiel Y, Ziv A, Bock Y, Fang P, Wdowinski S. 2012. Crustal deformation along the Dead Sea Transform and the Carmel Fault inferred from 12 years of GPS measurements. *J Geophys Res: Solid Earth* 117.
- Sarikaya A, Yildirim C, Ciner A. 2015. Late Quaternary alluvial fans of Emli Valley in the Ecemis Fault Zone, south central Turkey: insights from cosmogenic nuclides. *Geomorphology*, 228: 512–525
- Sengör AMC, Yalcin N, Canitez N. 1980. The origin of the Adana/Cilicia Basin. An incompatibility structure arising at the common termination of the Eastern Anatolian and Dead Sea transform faults, in: *Sedimentary Basins of Mediterranean Margins*. C.N.R. Italian Project of Oceanography, pp. 45–46.
- Sengör AM, Zabc C, Natal'in BA. 2019. Continental transform faults: congruence and incongruence with normal plate kinematics, in: *Transform plate boundaries and fracture zones*. Elsevier, pp. 169–247.
- Sançar T, Zabcı C, Karabacak V, Yazıcı M, Akyüz HS. 2019. Geometry and Paleoseismology of the Malatya Fault (Malatya-Ovacık Fault Zone), Eastern Turkey: Implications for intraplate deformation of the Anatolian Scholle. *J Seismol* 23: 319–340.
- Sengör A. 1979. The North Anatolian transform fault: its age, offset and tectonic significance. *J Geolog Soc* 136: 269–282.
- Sengör AMC, Görür N, Saroğlu F. 1985. Strike-Slip Faulting and Related Basin Formation in Zones of Tectonic Escape: Turkey as a Case Study1, in: Biddle KT, Christie-Blick, N. (Eds.), *Strike-Slip Deformation, Basin Formation, and Sedimentation. SEPM Society for Sedimentary Geology* 37: <https://doi.org/10.2110/pec.85.37.0211>.
- Toda S, Stein RS. 2024. The Role of Stress Transfer in Rupture Nucleation and Inhibition in the 2023 Kahramanmaraş, Türkiye, Sequence, and a One-Year Earthquake Forecast. *Seismolog Res Lett* 95: 596–606.
- Umhoefer PJ, Thomson SN, Lefebvre C, Cosca MA, Teyssier C, Whitney DL. 2020. Cenozoic tectonic evolution of the Ecemiş fault zone and adjacent basins, central Anatolia, Turkey, during the transition from Arabia-Eurasia collision to escape tectonics. *Geosphere* 16: 1358–1384.
- Viltres R, Jónsson S, Althman AO, Liu S, Leroy S, Masson F, Doubre C, Reilinger R. 2022. Present-day motion of the arabian plate. *Tectonics* 41: e2021TC007013.

- Walters RJ, Parsons B, Wright TJ. 2014. Constraining crustal velocity fields with InSAR for Eastern Turkey: limits to the block-like behavior of Eastern Anatolia. *J Geophys Res: Solid Earth* 119: 5215–5234.
- Wang K, Wells R, Mazzotti S, Hyndman RD, Sagiya T. 2003. A revised dislocation model of interseismic deformation of the Cascadia subduction zone. *J Geophys Res: Solid Earth* 108: <https://doi.org/10.1029/2001JB001227>.
- Weiss JR, Walters RJ, Morishita Y, Wright TJ, Lazecky M, Wang H, Hussain E, Hooper AJ, Elliott JR, Rollins C, Yu C, González PJ, Spaans K, Li Z, Parsons B. 2020. High-resolution surface velocities and strain for anatolia from Sentinel-1 InSAR and GNSS Data. *Geophys Res Lett* 47: e2020GL087376.
- Welford JK, Hall J, Rahimi A, Reiche S, Hübscher C, Loudon K. 2015. Crustal structure from the Hecataeus Rise to the Levantine Basin, eastern Mediterranean, from seismic refraction and gravity modeling. *Geophys J Int* 203: 2055–2069.
- Westaway R. 2003. Kinematics of the Middle East and eastern Mediterranean updated. *Turk J Earth Sci* 12: 5–46.
- Yildirim C, Sarikaya MA, Çiner A. 2016. Late Pleistocene intraplate extension of the Central Anatolian Plateau, Turkey: inferences from cosmogenic exposure dating of alluvial fan, landslide, and moraine surfaces along the Ececi Fault Zone. *Tectonics* 35: 1446–1464.
- Özkan A, Yavaşoğlu HH, Masson F. 2023. Present-day strain accumulations and fault kinematics at the Hatay Triple Junction using new geodetic constraints. *Tectonophysics* 854: 229819.

**Cite this article as:** Özbey V, Sengör AMC, Henry P, Özeren MS, Haines AJ, Klein EC, Tarı E, Zabcı C, Chousianitis K, Güvercin SE, Öğretmen N. 2024. Kinematics of the Kahramanmaraş triple junction and of Cyprus: evidence of shear partitioning, *BSGF - Earth Sciences Bulletin* 195: 15.